A Viable Orbital Debris Mitigation Mission using Active Debris Removal

Stanley L. Smeltzer

Thesis submitted to the faculty of the
Virginia Polytechnic Institute and State University
in partial fulfillment of the requirements for the degree of

Master of Science
in
Aerospace Engineering

Rakesh K. Kapania, Chair
Riley M. Fitzgerald
Samantha P. Kenyon

April 26, 2023
Blacksburg, Virginia

Keywords: orbital debris, active debris removal, MATLAB, STK

A Viable Orbital Debris Mitigation Mission using Active Debris Removal

Stanley L. Smeltzer

ABSTRACT

Currently, the Low Earth Orbit (LEO) space environment contains a growing number of orbital debris objects. This growing orbital debris population increases collision probabilities between both orbital debris and functioning satellites. A phenomenon known as Kessler Syndrome can be induced if these collisions occur. Kessler Syndrome states that these collisions can lead to an exponential increase in the orbital debris population, which could dangerously impede future space missions. Current literature outlines the necessity of stabilizing the near-Earth environment debris population and introduces the concept of active debris removal (ADR). The use of ADR on five orbital debris objects per year was found to be a requirement to achieve stability within the orbital debris population. A viable mission architecture is henceforth explored to utilize ADR for near-future execution to further develop research for orbital debris mitigation missions. The larger orbital debris objects are found in many different orbital regimes and are primarily composed of spent rocket bodies and retired satellites. Different orbital debris ranking schemes have been developed based on the population density in these different regimes, which are linked to higher collision probabilities. Using these ranking schemes, a set of target objects are selected to be investigated for this mission design that was composed of target objects with

similar orbital characteristics that were not launched by the Commonwealth of Independent States (CIS) to minimize legal barriers. Different ADR capture and removal methods are inspected to find the optimal methods for this mission. An Analytical Hierarchy Process (AHP) has been used to assess these different methods, which utilizes comparisons of the different methods among a set of weighted criteria. A net capture method with a low thrust chemical engine for removal is identified as the optimal ADR method. The use of a laser detumbling system is also selected to stabilize target objects with a high rotation rate. A rendezvous and deorbit orbital analysis are conducted using both a low fidelity tool (for preliminary results) and a high fidelity tool (for more precise results). The rendezvous analysis is used to select a mission architecture that was composed of two different chaser satellites which rendezvous with the five different target objects by taking advantage of nodal precession. The deorbit analysis investigates different decay timelines and found the delta-v estimates that would be required to deorbit the target objects within the same year that they were captured in. These two orbital analyses provide valuable insight to the mission timeline, delta-v estimates, and approximate mass requirement for the chaser satellite and deorbit kits. The results of the target selection process, ADR selection process, and the rendezvous and deorbit analyses are meant to provide an initial concept and analysis for a near-future ADR mission. These approximate results provide insight and information to further develop orbital debris mitigation research to help solve the orbital debris population growth challenge for future space missions.

A Viable Orbital Debris Mitigation Mission using Active Debris Removal

Stanley L. Smeltzer

GENERAL AUDIENCE ABSTRACT

Currently, the near Earth space environment contains a growing number of space debris. This growth in the orbital debris population increases the likelihood of collisions with orbital debris, functioning satellites, and launch vehicles. These collisions can generate a chain of events that could exponentially increase the population of orbital debris, which at some scale could become a major obstacle for future space missions. Researchers have introduced the concept of active debris removal (ADR), which in simulations has been shown to help stabilize the growth of orbital debris. The use of ADR to remove as low as five orbital debris objects per year has been found to be sufficient to stabilize debris growth. A viable mission architecture using ADR technologies that can be implemented in the near future is henceforth explored to further develop research for orbital debris missions. The larger orbital debris objects are found in many different areas in space and are primarily made up of used rocket bodies and retired satellites. Different ranking schemes have been developed by researchers for these larger orbital debris objects based on the population density within these areas in space, which are linked to the chance of a collision. Using these ranking schemes, a set of orbital debris objects are selected to be targeted for this mission design. This set of selected target objects have similar orbital characteristics and

the political/legal barriers that could be present during removal are minimal. An ADR mission is composed of two primary components, a capture method and a removal method, which are inspected to find the optimal methods for this mission. A decision-making technique, called an Analytical Hierarchy Process (AHP), has been used to assess these different methods. The AHP compares different capture and removal methods using a set of weighted criteria. A net capture method with small thrusters for removal is identified as the optimal ADR method. Additionally, the use of a laser system is selected to stabilize target objects that may be rotating too quickly for capture. An analysis on different mission architectures is conducted using both a low fidelity tool (for preliminary results) and a high fidelity tool (for more precise results). A mission architecture composed of two different "chaser" satellites which rendezvous with and deorbit the five different target objects is selected. The analysis used on the selected mission architecture provides valuable insight to the mission timeline, fuel estimates, and approximate mass requirements. The results of the target selection process, ADR selection process, and the mission architecture analysis are meant to provide an initial concept and introduce possible requirements for a near-future ADR mission. These approximate results provide information to further develop research that can help us solve the orbital debris population growth challenge for future space missions.

Acknowledgements

This thesis would not have been possible without the assistance from many different people. Thank you to my faculty advisor Dr. Rakesh K. Kapania for all of your guidance throughout the past two years. Thank you to my committee, both Dr. Samantha Kenyon and Dr. Riley Fitzgerald, for meeting with me on numerous occasions and providing valuable insight into my work. Thank you to all of my friends and family that supported and encouraged me throughout this process. Thank you to the College of Engineering Dean's Office for supporting me through my graduate school journey. Additionally, thank you to all of the faculty and staff within the Aerospace and Ocean Engineering Department that made my education possible.

Table of Contents

List of Figures

List of Tables

List of Abbreviations

a	Semimajor Axis
a_{d}	Acceleration Due to Drag
A	Surface Area
c_{d}	Coefficient of Drag
C	Series Function
Δv	Delta-V
e	Eccentricity
E	Eccentric Anomaly
f	Lagrange Function
F	Hyperbolic Anomaly
g	Lagrange Function
g_{o}	Gravitational Constant of Earth
i	Inclination
I_{sp}	Specific Impulse
J_2	Earth's Oblateness Constant
k	Universal Iterate Variable
m	Mass
m_{f}	Final Mass
m_{prop}	Propellant Mass
M	Mean Anomaly

n	Mean Motion
ω	Argument of Perigee
$\dot{\omega}$	Precession of Perigee
Ω	Right Ascension of the Ascending Node
$\dot{\Omega}$	Nodal Precession
ρ	Atmospheric Density
r	Radius
R_{Earth}	Radius of the Earth
S	Series Function
t	Time of Flight
μ	Gravitational Parameter of Earth
ν	True Anomaly
v	Velocity
x	Universal Variable
z	Universal Variable
ADR	Active Debris Removal
AFB	Air Force Base
AGI	Ansys Government Initiatives
AHP	Analytical Hierarchy Process
CIS	Commonwealth of Independent States
DAS	Debris Assessment Software
EOL	End of Life
EOY	End of Year

GEO	Geostationary Orbit
HPC	Hohmann Transfer with Plane Change
IADC	Inter-Agency Space Debris Coordination Committee
LEO	Low Earth Orbit
MCS	Mission Control Sequence
MEO	Medium Earth Orbit
MM	Million
MMH	Monomethylhydrazine
NTO	Dinitrogen Tetroxide
PRC	People's Republic of China
RAAN	Right Ascension of the Ascending Node
RIC	Radial, In-Track, Cross-Track
SGP4	Simplified General Perturbations Propagator
SMC	Statistically Most Concerning
SPOUA	South Pacific Ocean Uninhabited Area
SSO	Sun-Synchronous Orbit
STK	Systems Tool Kit
TLE	Two-Line Element Set
TOF	Time of Flight
TRL	Technology Readiness Level
V&V	Verification and Validation

Chapter 1

Introduction

1.1 Background

There are over 500,000 pieces of orbital debris that are estimated to be orbiting Earth that are larger than 1 cm. Approximately 23,000 of these pieces of orbital debris are 10 cm or larger and are located in Low Earth Orbit (LEO). These are being tracked by the Space Surveillance Network. This high number of orbital debris objects pose a serious threat towards future space missions. A collision between an orbital debris object and a functioning space system could result in a mission failure. In fact, even the smallest sizes of these orbital debris objects, on the millimeter scale, can cause damage to a functioning space system [1].

If either a functioning space system or piece of orbital debris collide with one another, a phenomenon known as Kessler Syndrome could occur. Kessler Syndrome states that collisions that occur in the near-Earth environment can lead to an exponential increase in the orbital debris population. This exponential increase in the orbital debris population can increase without the addition of other space objects. These collisions could create orbital

regimes with very high orbital debris densities which could become unusable for future space missions [2].

The United States government and the United Nations have both created new guidelines in response to this growing issue. Mandatory guidelines to the end-of-life (EOL) procedures for future missions have been created, for international and domestic missions, in an attempt to stop the growth of orbital debris [3][4]. International committees, such as the Inter-Agency Space Debris Coordination Committee (IADC), have created additional guidelines to further mitigate the debris population issue [5]. Even collections of commercial organizations have developed best practice documents to show private-sector support of these issues and help provide insight to possible solutions [6].

The orbital debris population has spurred many different fields of research. Comparisons of different EOL technologies and advances in collision avoidance systems have been investigated to be used as orbital debris mitigation techniques [7][8]. Additionally, researchers have been using simulations to further understand how the future orbital debris population will grow and evolve. A 2010 study has shown that an increase in the LEO orbital debris population is unavoidable. Additionally, this analysis concludes that the use of active debris removal (ADR) is necessary to stabilize the population of orbital debris in LEO [9].

A continuation of this study found a projected population growth for orbital debris objects larger than 10 cm in LEO, medium Earth orbit (MEO), and geostationary orbit (GEO) if no mitigation measures were utilized (Fig. 1). This exponential growth can be reduced due to the end-of-life requirements that have been developed, but additional mitigation measures such as ADR are still required to stabilize the LEO environment.

Different ADR rates were analyzed to find the number of objects that would need to be removed per year for LEO stabilization, including a 90% success rate of end-of-life operations ending in post mission disposal (Fig. 2). Removing approximately five pieces of orbital debris per year using ADR, while continuing to utilize post mission disposal, was found to stabilize the population of orbital debris objects in LEO [10].

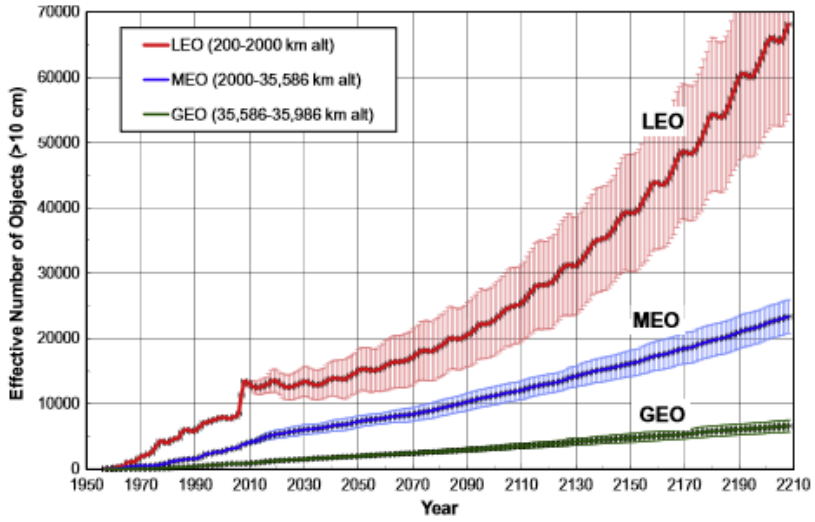

Figure 1: Orbital Debris Population for Different Orbit Regimes [10].

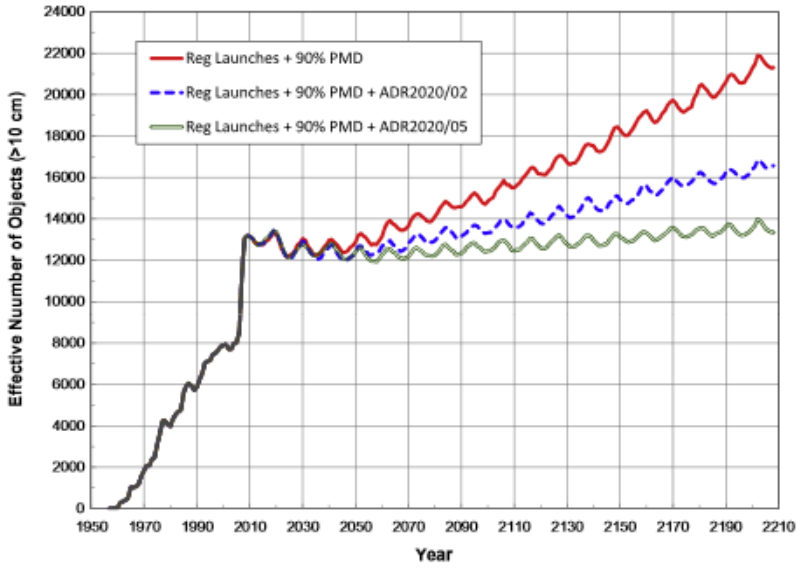

Figure 2: Effects of ADR on the Orbital Debris Population in LEO. The effects on the debris population by removing 0, 2, and 5 objects using ADR is illustrated [10].

After ADR was accepted as a necessary route for future missions, ADR research significantly increased. Different ranking schemes were developed for orbital debris objects found in LEO and many different ADR techniques were introduced, investigated, and compared. This research was necessary to begin designing ADR missions and to continue to find additional areas of research that must be explored. Current ADR missions have been designed to take advantage of electric propulsion [11], hybrid propulsion [12], low-thrust propulsion [13], and even drag sails [14]. Additionally, missions have been designed that focus on the removal of multiple debris objects [15][16].

1.2 Problem Definition

The objective of the following paper is to further expand research in the field of orbital debris mitigation, specifically ADR mission designs. Three different trade studies were analyzed to develop a new ADR mission design. These trade studies sought to review previous works, and select a set of orbital debris targets, choose an ADR method, and use an orbital mechanics analysis to select a mission architecture. The objective of the selected final mission architecture is to be a viable orbital debris mitigation mission design that can be further analyzed and implemented in the near future to slow the orbital debris population growth. Additionally, the results of these trade studies can provide valuable insight for future research and mission designs.

1.3 Mission Requirements

A set of high-level mission requirements were developed to be used throughout the different analyses (Fig. 3). To ensure that the final mission design will be a viable option

for implementation in the near future, requirements were set to minimize mission cost and not to create legal barriers. To uphold the mission objective to slow the orbital debris population growth, requirements were established to remove five orbital debris objects, achieve rendezvous in less than one year, and minimize mission timeline. These requirements attempt to satisfy the conditions given by Liou et al. [10], which is necessary to achieve stabilization in the LEO orbital debris population.

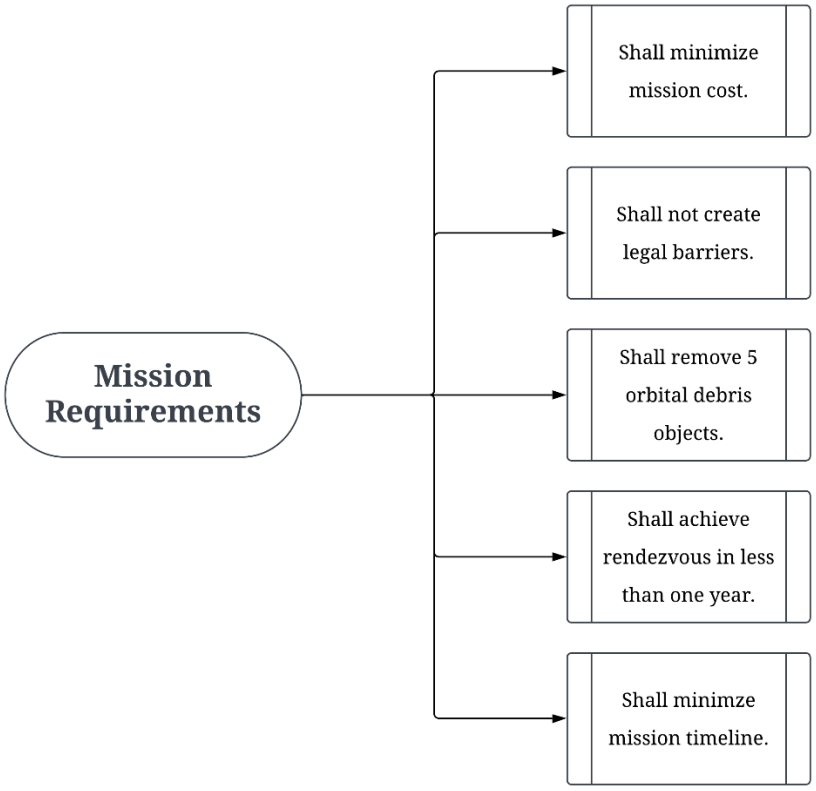

Figure 3: Mission Requirements Diagram.

Chapter 2

Target Selection

2.1 Target Selection Methods

Different methods of ranking space debris have occurred over recent years. These ranking schemes provide insight for potential target candidates in future ADR missions. The mass density and altitude of tracked space debris was used to identify the most favorable regimes for ADR missions. Researchers found that 600 km, 800 km, and 1000 km were the altitudes that had the highest mass density of objects (Fig. 4). The objects in these regions primarily consist of upper stages of rocket bodies and non-operational spacecraft. This information is crucial for identifying which debris objects have the highest probability of collision.

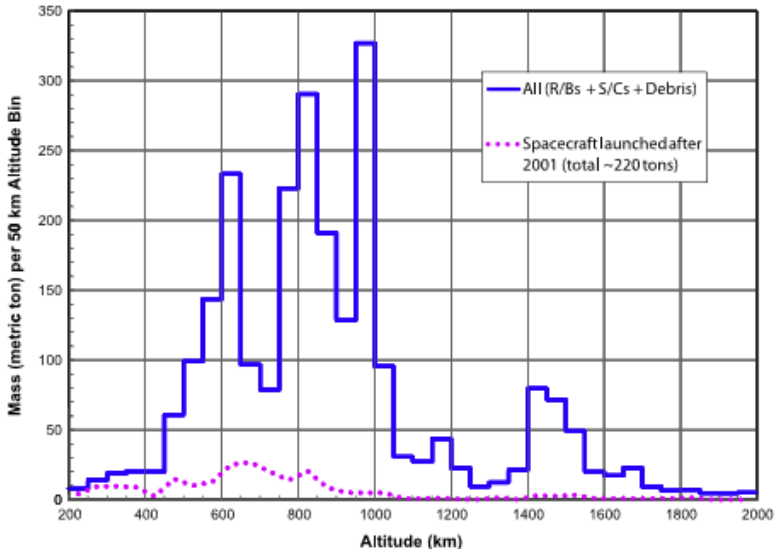

Figure 4: Orbital Debris Mass Distribution in LEO [10].

A ranking scheme was developed for intact upper stages of rocket bodies found in LEO. These upper stages were compared by a ranking index that was derived from the collision probability of these upper stages. The collision probability is evaluated using the flux of orbital debris in the upper stage's orbital plane and the upper stage's cross-sectional area. The results of this ranking scheme found that among all of the upper stages in LEO, only five upper stage types made up almost 75% of the rocket body mass under 2,000 km. Additionally, the Zenit-2 second stage was found to hold the highest ranking and displayed a large environmental criticality to the LEO environment [17]. The Zenit-2 second stages were launched by the Commonwealth of Independent States (CIS) which is of Russian origin.

Another ranking index was developed which applied to all LEO orbital debris objects, including rocket bodies and decommissioned satellites. This ranking criterion utilized environmental, economic, operability, and mission related indices for orbital debris object comparisons. As with the upper stage ranking scheme, the debris flux was a primary

measurement that was used for locating high collision probability regimes (Fig. 5). The results of this ranking index also found that the highest ranked objects were dominated by the Zenit-2 second stage, although it also found the satellite Envisat was ranked third among all the LEO orbital debris objects [18].

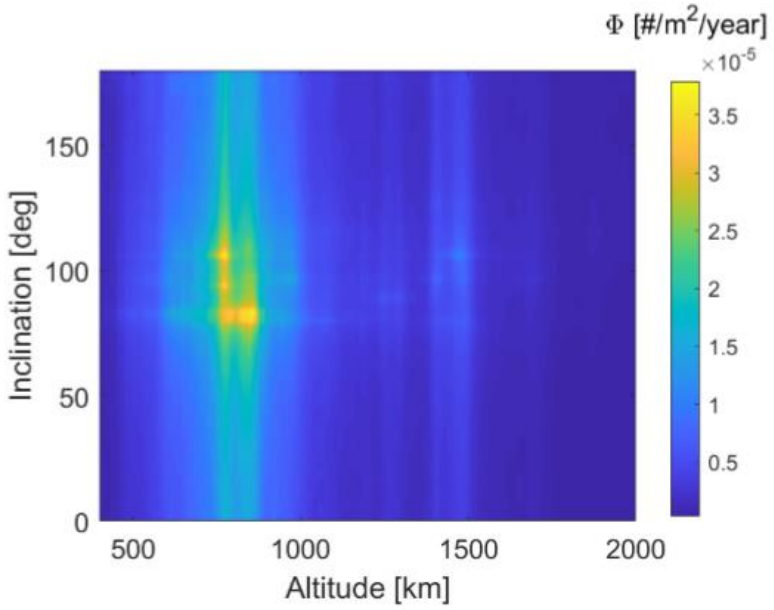

Figure 5: Orbital Debris Flux as a Function of Inclination and Altitude [18].

Due to the growing number of unique ranking methods and indexes, a "superior aggregate model" was developed by combining 11 different ranking methods to find the statistically most concerning (SMC) objects in LEO. This model evaluated 11 ranking schemes and found the top 50 ranked objects that resulted from using each independent method. These results were combined which gave each orbital debris object a SMC score. These scores were dominated by the number of lists that each object was found on, as well as the placement in each list. The results of this model are similar to past results which find the dominance of the Zenit-2 second stage [19].

The country of origin of these highest ranked debris objects is a concern when creating a target list of debris objects for ADR missions. The Zenit-2 second stages were found to dominate most ranking method's results which are of Russian origin. This could create legal issues if these objects were selected for an ADR mission. This issue may arise from the Outer Space Treaty and Liability Convention which states that both working and retired space debris objects are held under liability of the state from which the space debris object was launched [20]. This suggests that diplomatic relations may be required if certain debris objects are selected for an ADR mission.

A recent study ran different simulations to understand the practicality of these ranking schemes. The highest ranked objects were chosen for removal and the impact to the debris object population growth was found. Additionally, the debris object rankings were found to change as different debris objects were removed. It was concluded that starting ADR missions as soon as possible has a higher impact on stabilizing the debris population as compared to targeting the highest ranked objects [21].

Additionally, further research was conducted to find the interaction between ADR rates and the debris object population. This research concluded that the effectiveness of ADR as it interacts with the debris population growth diminishes with an increased rate of ADR [22]. This suggests that the minimum number of high ranked debris objects should be chosen in order for ADR missions to continue to be effective in stabilizing the LEO debris population. Otherwise, with current technologies, the cost of these ADR missions would grow to exceed their benefit.

2.2 Target Analysis

The first trade study will identify a set of target objects that will be used for this ADR mission. The top 50 SMC objects were used as the primary ranking results as discussed in the previous section. This list was chosen since it was an aggregate analysis that combined the results of many previous ranking schemes. Additionally, this set of target objects must fulfill the mission requirements by creating a set of five orbital debris target objects and should not create legal barriers.

The first target grouping is composed of the top five ranked SMC objects (Table 1). These top five targets are all found to have similar orbital properties such as apogee, perigee, and inclination. The apogee and perigee measure the distance that a debris object's orbit is located away from Earth. The apogee is the furthest distance that the orbit reaches from the Earth while the perigee is the shortest distance that the orbit reaches from the Earth. The inclination gives insight into the debris object's orbital plane. Additionally, these debris objects are found to be of CIS origin which could impose a potential legal barrier. International cooperation is ideal for solving the global orbital debris problem, though liability policy could potentially restrict removal of the Russian Zenit-2 stages.

Table 1: Top 5 Overall SMC Objects. All these objects are SL-16 R/B which is a Zenit-2 second stage that was launched by the CIS. Notice the similar apogee, perigee, and inclination among all five objects [19].

Top 5 Overall	SMC Rank	Mass (kg)	Country	Apogee (km)	Perigee (km)	Inclination (deg.)
22566 SL-16 R/B	1	9000	CIS	848	836	71.01
22220 SL-16 R/B	2	9000	CIS	847	827	71
31793 SL-16 R/B	3	9000	CIS	845	843	70.97
26070 SL-16 R/B	4	9000	CIS	854	827	71
16182 SL-16 R/B	5	9000	CIS	844	832	71

To continue to comply with our mission requirement not to create legal barriers, a second target grouping is introduced. This second target grouping is composed of the top five SMC targets that were not launched by the CIS or the People's Republic of China (PRC) (Table 2). These debris objects were all launched by countries that regularly cooperate with one another in the space domain.

Table 2: Top 5 Non-CIS/PRC SMC Objects. All these objects were launched by countries that regularly cooperate in the space domain. Notice the similar inclination, however the apogee and perigee values for H-2 R/B are over a wide range [19].

Top 5 Non-CIS/PRC	SMC Rank	Mass (kg)	Country	Apogee (km)	Perigee (km)	Inclination (deg.)
27386 ENVISAT	21	7800	ESA	765	764	98.2
24277 ADEOS	23	3560	JPN	795	792	98.94
27601 H-2A R/B	24	3000	JPN	835	734	98.18
24279 H-2 R/B	28	2700	JPN	1306	859	98.77
27597 ADEOS 2	34	3680	JPN	801	798	98.62

Similarly, to the first target grouping, this group of debris objects are close in inclination. However, the apogee and perigee of the H-2 R/B are not alike. Keeping the orbital characteristics of the debris objects as similar as possible is important help minimize the delta-v, which is the change in velocity required to move from an initial orbit to a new desired orbit, required to rendezvous with the different debris objects. Creating a target grouping with similar orbital characteristics allows for more flexible and optimal mission architecture designs.

Adjusting the top five SMC object list that are of non-CIS/PRC origin led to the development of a third target grouping (Table 3). These objects have less than one deg. difference in inclination, less than 75 km difference in apogee, and less than 65 km difference in perigee. These orbital characteristics are very similar to each other and are all not of CIS or PRC origin. Additionally, although these target objects are not the very highest ranked among the top 50 list SMC objects, each of these target objects are still located in the top 50 of SMC objects.

Table 3: Top 5 Non-CIS/PRC Adjusted SMC Objects. All these objects were launched by countries that regularly cooperate in the space domain. Notice the similar apogee, perigee, and inclination among all five objects [19].

Top 5 Non-CIS/PRC Adjusted	SMC Rank	Mass (kg)	Country	Apogee (km)	Perigee (km)	Inclination (deg.)
27386 ENVISAT	21	7800	ESA	765	764	98.2
24277 ADEOS	23	3560	JPN	795	792	98.9
27601 H-2A R/B	24	3000	JPN	835	734	98.18
27597 ADEOS 2	34	3680	JPN	801	798	98.62
27387 ARIANE 5 R/B	39	2575	FR	796	748	98.6

2.3 Target Selection

The third group of five debris objects were selected to be used as target objects for this ADR mission. The elimination of the CIS and PRC originated debris objects should avoid political liability concerns to comply with the mission requirements. The similarity in the selected set of target object's orbital characteristics should allow for the design of an optimal design architecture. As previously discussed, the target rankings do not influence the stabilization of orbital debris population as much as the need to begin ADR missions immediately. This selection attempts to create a set of target objects for an ADR mission that can be executed as soon as possible as opposed to waiting longer to execute a mission to remove the top five ranked SMC objects. In the future, if permission was granted to remove the CIS satellites, it would be obvious to use the first target grouping that holds the top five SMC objects while also having similar orbital characteristics.

Chapter 3

Active Debris Removal Selection

3.1 Active Debris Removal Techniques

There are many different techniques that are being researched and developed to be used for ADR missions. Understanding the current research in different ADR techniques, as well as investigating current comparisons between ADR techniques, is essential. There are two primary categories when discussing these ADR techniques. The first category is the method used to capture the target object. The second category is the method used to remove the target object from its current orbit to a desired location. These removal methods can range from deorbiting the target object to transferring them to a graveyard orbit, which are particular orbits that are reserved for non-operational space systems.

Additionally, detumbling is critical in some ADR scenarios. Some target objects may have naturally acquired a high rotation rate due to different orbital perturbations, which are different phenomenon that affect the motion of space systems. One perturbation that could have an influence on the rotation rate is the drag effects on a non-uniform surface area. If the capture method requires a low rotation rate, de-tumbling must be performed until the target object's rotation rate has decreased to a level that will allow the capture method to perform.

3.1.1 Capture Methods

Within the different capture methods, there are two primary groupings: contact capture methods and contactless capture methods. The contact capture methods require direct contact with the target object while the contactless capture methods utilize gravitational or electrostatic effects for capture (Fig. 6). Contact capture methods can be executed by either a stiff connection system such as a robotic arm or a flexible connection system which commonly use a space tether for connection. Contactless methods are in very early stages of design and are not currently designed to be used on larger target objects, thus these methods are not investigated further [23].

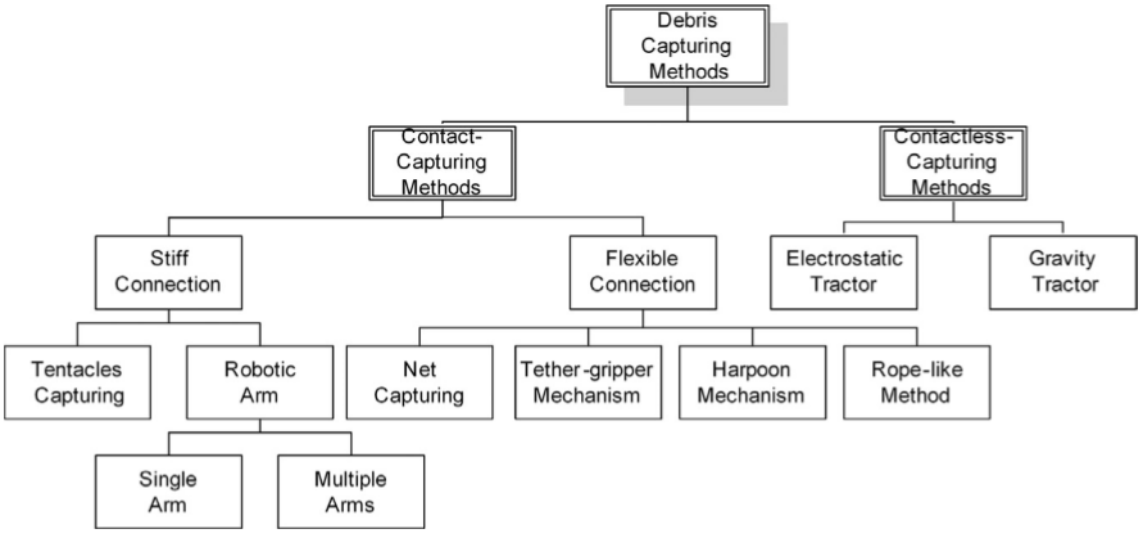

Figure 6: Different Debris Capture Methods [23].

To further develop ADR capture methods, a mission named RemoveDEBRIS sought to demonstrate two different capture technologies in orbit [24]. A net capture system and a harpoon capture system were developed while implementing a navigation system to target the target object. This was one of the first missions that attempted to take these different ADR capture methods out of lab testing to demonstrate their on-orbit capabilities while

also designing for a low-cost mission [24]. Implementation of these contactless methods, especially methods that utilized a flexible connection system, spurred further research into the dynamics of these flexible connection systems and their design for ADR missions [25].

As different capture methods became more fully developed, comparison studies began between the different methods. These comparison studies attempted to provide comparisons metrics such as: method robustness, removal capabilities, mission cost, technology readiness level (TRL), mission risk, and the propellant mass that would be required. One specific study utilized two separate comparison metrics, an analytical metric and a utility metric, to compare a subset of ADR methods. The results of this study found that there was a high potential for net capture systems and robotic arm capture systems in future ADR missions [26].

A recent study conducted an in-depth review of different contact and contactless capture methods. Each capture method is discussed, and previous literature is cited for their current designs, analysis, and applications (Table 4). Many different robotic arm configurations have been developed due to the high uncertainty of target object's shapes. A major disadvantage of the robotic arm is that implementation requires a very low tumbling rate. The net capture method is advantageous since it may deploy at a distance to the target object. Additionally, the net capture method may be used for many different target object configurations and can even be used on some tumbling target objects. Many different studies have investigated optimal net configuration, deployment techniques, and tumbling rate requirements. Tethered space robots may also be deployed at a distance from the target object, however, has very complex control requirements. The harpoon capture method continues to take advantage of a flexible connection system. A harpoon attached

to the end of a space tether system can solve the tumbling issue by hitting a desired point on the target object which can significantly slow the tumbling rate of the target object while also connecting with the target object. The primary disadvantage to this technique is the possibility of the creation of additional space debris during the penetration of the harpoon [27].

Table 4: Types of Contact and Contactless Capture Methods [27].

Contact Capture Methods	Contactless Capture Methods
Robotic Arms	Ion Beam
Nets	Electrostatic
Tethered Space Robots	Gravitational
Harpoons	

3.1.2 Removal Methods

Removal methods can utilize the space environment that is present in the target objects orbital regime or can originate from more active removal systems (Fig. 7). Many of these removal methods depend on the target object's size and location. Most space environment-based systems and contactless removal methods are used for smaller target objects or target objects that are at a very low altitude. Contact methods, however, can target larger objects for removal [23]. The use of a drag sail for deorbiting capabilities, a space environment-based method, was designed to be demonstrated on a target object that had a low altitude and low mass [24].

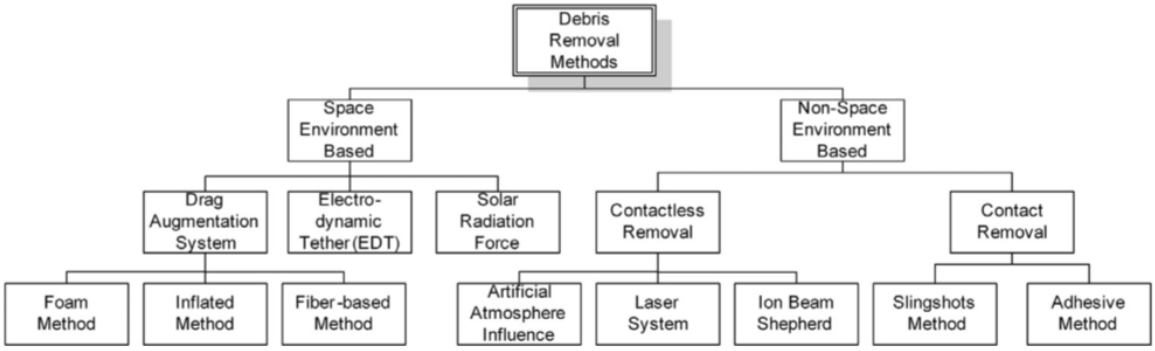

Figure 7: Different Debris Removal Methods [23].

A review of the different removal methods provides valuable insight into proposed applications and current analyses on these different methods. Different contact and contactless methods were reviewed (Table 5). Conventional thrusters require a hard grip connection with the target object and are extensively researched and analyzed. Due to the high thrust of these conventional thrusters, elastic structures on the target object could lead to fragmentation which could generate additional space debris. Low thrust engines can be utilized if a space tether is used to capture the target object. These capabilities are being researched for implementation of necessary control laws that are required for effective towing [27].

Table 5: Types of Contact and Contactless Removal Methods [27].

Contact Removal Method	Contactless Removal Method
Conventional Thrusters	Drag Augmentation
Low Thrust Engines	Lasers
Electrodynamic Tethers	
Momentum Exchange	
Inflatable Balloon	
Solar Sails	

Electrodynamic tethers take advantage of the Earth's magnetic field by generating a current through a long conducting tether. This method is a lightweight option with implementation open to many different orbital regimes, but the long tether creates a higher probability of collision between other pieces of space debris. A momentum exchange uses the laws of Newtonian mechanics to decrease the altitude of a target object by generating angular momentum. This angular momentum is generated by shortening and elongating the tether connection between the removal system and the target object to induce a rotation. This system can increase the effectiveness of ADR missions by requiring less fuel to deorbit target objects. Inflatable balloon systems and solar sails both utilize environmental effects to change the orbit of target objects. The major disadvantage to both of these systems is due to their very high cross-sectional area that is necessary for these systems to use. These high cross-sectional areas significantly increase their collision probability with surrounding objects since the target objects are located in regions of higher debris densities [27].

3.1.3 Detumbling

Finding solutions to capture target objects that are tumbling is necessary for many ADR techniques. An added complication to this problem is that there is high uncertainty in the majority of target object's tumbling rates. Additionally, natural forces can gradually change these tumbling rates over time. A technique was investigated on grasping a target object that had a non-zero angular rotation rate [28]. A brush contactor attached to a robotic arm was discussed as another technique to reduce the angular rotation rate of a target object to allow for capture [23]. Furthermore, a broader application of a detumbling technique was

proposed using laser ablation. Laser ablation uses a laser beam to break down the surface of a specified point on a target object generating a force that can be used to detumble a target object [29].

3.2 Active Debris Removal Analysis

The trade study for ADR technique selection utilized an Analytical Hierarchy Process (AHP). The previous capture and removal methods that have been introduced, as well as additional methods found throughout the literature, were compared against each other. This comparison sought to find the best ADR technique to be used given our previously selected set of target objects. Due to the large size of this set of target objects, most contactless methods such as ground based lasers, space-based lasers, drag augmentation, and ion beams were not further analyzed.

3.2.1 Analytical Hierarchy Process

An AHP makes a pairwise comparison among different design choices to find a solution given specified criteria. This analytical method uses judgement to rank the different criteria based on the mission objectives. Using an AHP is an effective tool for measuring mission specific characteristics or for user specified metrics. Additionally, a previous study used an AHP model as an assessment technique to measure different ADR methods against each other [26].

The AHP used in this trade study compares each criterion against one another to generate a pairwise comparison matrix. These comparisons illustrate the importance of one criterion over the other. This matrix is squared, and values are summated in each criterion

row. After this summation, the values are normalized, and the result provides a weighting value for each criterion. The different capture and removal methods are then analyzed in a similar pairwise comparison against each of the criteria. The results of the pairwise comparisons are combined with each criterion weighting value. After these values have been normalized, the new totals can be measured against one another and ranked. The highest-ranking methods are thus suggested to be the "best" choice for the provided criterion [26].

3.2.2 Capture Method Analysis

An AHP was used to identify the optimal capture method for this mission given a specified criterion. The criterion that was used to evaluate different capture methods using an AHP was robustness (capability to execute in a wide variety of scenarios), simplicity, technology readiness level, volume required for the capture method, mass, and risk. Each of these criteria had either a minimization or maximization goal. For this mission, the goal was to maximize robustness, simplicity, and TRL while minimizing the volume required, mass, and risk.

A weighting factor was developed for each criterion after completing the first steps of the AHP (Table 6). The top three criteria were found to be the risk, volume required, and the TRL. The risk associated with the mission is weighted heavily since failure could reciprocate the effectiveness of an ADR mission by creating additional space debris instead of removing target debris. It is very important for this mission to decrease the amount of volume that is required of any single capture method. Additionally, choosing a capture

method with a higher TRL does not require additional time for the selected capture method to be researched so as to be utilized on a mission.

Table 6: Capture Method Criterion Weightings developed via a Pairwise Comparison. The risk, volume required, and the TRL of the capture method were found to have the highest weightings.

Criterion	Weightings
Robustness	0.14
Simplicity	0.12
Volume Required	0.21
Mass	0.11
TRL	0.20
Risk	0.22

The capture methods that were investigated in this analysis were single arm, multiple arms, tentacle, net, harpoon, and tether-gripper capture. The single arm, multiple arm, and tentacle capture methods are different types of robotic grasping mechanisms. The net capture method utilizes the deployment of a net to capture the desired target object. The harpoon capture method shoots a harpoon at a desired location on a target object to capture. The tether-gripper capture method, like tethered space robots, uses a grasping mechanism on the end of a space tether to capture the desired target object.

A ranking of the different capture methods was developed using the AHP by comparing them against the different criteria (Table 7). The net capture method was ranked first with a score of 0.23 while the single arm capture method was ranked second with a score of 0.21. The net and single arm capture methods had a very similar score. The net method is the preferred capture method given these results. However, the single arm capture method

will be used if the net capture system cannot be integrated with either of the top two removal methods.

Table 7: Rankings of the Different Capture Methods. The top two capture methods were found to be the single arm capture and the net capture methods.

Capture Method	Score
Tentacle	0.06
Single Arm	0.21
Multiple Arms	0.13
Nets	0.23
Tether-Gripper	0.17
Harpoon	0.19

3.2.3 Removal Method Analysis

Similarly to the capture method, an AHP was used to find the optimal removal method for this mission. The criterion that was developed to compare the different removal methods are power required, robustness, simplicity, volume required, mass, TRL, and risk. Goals of maximization were set to robustness, simplicity, and TRL while minimizing power required, volume required, mass, and risk. Maximizing robustness, simplicity, and TRL allow for the mission to be executed in the near future while maintaining flexibility in the mission architecture. Minimizing power required, volume required, mass, and risk are necessary to fit the desired launch vehicle specifications and perform a successful removal of the target objects.

After completing a pairwise comparison of the different criterion, the respective weightings were computed using the AHP methodology (Table 8). The criterion with the

highest weighting was found to be the risk associated with the removal method. The risk associated with the capture method is important to ensure that the target object will be successfully removed from and not generate additional space debris. The volume required was found to be the second highest criteria due to the size constraints that could be present in the launch vehicle or ADR system. The TRL was also found to have a high weighting factor to keep the technology development timeline to a minimum.

Table 8: Removal Method Criterion Weightings developed via a Pairwise Comparison. The risk, volume required, and the TRL of the capture method were found to have the highest weightings.

Criterion	Weightings
Power Required	0.04
Robustness	0.12
Simplicity	0.08
Volume Required	0.19
Mass	0.09
TRL	0.18
Risk	0.30

There are many different removal methods that can be implemented once the target object has been captured. It is important to keep in mind the size of the chosen set of target objects. The masses of these objects are large therefore we can disregard many different contactless and space environment-based removal methods such as solar radiation force, artificial atmosphere, and drag augmentation methods (inflatable balloon). The removal methods that have been chosen to be analyzed in the removal method AHP are electrodynamic tethers, momentum exchange, chemical engines, low thrust chemical engines, electric propulsion, and hybrid propulsion methods. The low thrust chemical

engines method utilizes smaller thrusters, compared to the chemical engine method, that can be used in conjunction with a space tether.

Completing the AHP analysis, the removal methods were ranked with respect to the previously discussed criterion. The chemical engine method was ranked first with a score of 0.22, and the low thrust chemical engines method was ranked second with a score of 0.20 (Table 9). The chemical engine method is assumed to be used with a grasping capture method while the low thrust chemical engines method is used with a space tether. The top two ranked removal methods will be investigated to find the optimal choice that will integrate with the capture method.

Table 9: Rankings of the Different Removal Methods. The top two removal methods were found to be chemical engines and low thrust chemical engines.

Removal Method	Score
Electrodynamic Tethers	0.18
Momentum Exchange	0.11
Chemical Engine	0.22
Low Thrust Chemical Engines	0.20
Electric Propulsion	0.14
Hybrid Propulsion	0.15

3.2.4 Detumbling Method

The tumbling rates of this mission's target objects require investigation to select the best detumbling method. These target objects had a wide variety of tumbling rates, some of which were stable and others that were rotating at a rate of almost 3.0 deg. per

second (Table 10). The highest rotation rate of the target objects was found to be Envisat which was estimated to rotate at a rate of 2.9 deg. per second with a spin period of roughly 124 seconds [30]. The second highest rotation rate was found to be ADEOS 2 which was estimated to rotate at a rate of 1.5 deg. per second [31]. The rates of ADEOS and the ARIANE 5 R/B were found to be much lower, and the rotation rate of the H-2A R/B was not found in current publications.

Table 10: Target Object's Rotation Rates. Envisat and ADEOS 2 were found to have a higher rotation rate while ADEOS and ARIANE 5 R/B were found to have very low rotation rates [30][31][32].

Target	Rotation Rate (deg./s)
27386 ENVISAT	2.9
24277 ADEOS	0.4
27601 H-2A R/B	Not found
27597 ADEOS 2	~1.5
27387 ARIANE 5 R/B	Stable

These tumbling rates are only approximations that were found using different techniques which are being developed to find debris object's tumbling rates. There is a high uncertainty in these measurements as well as the rate of change of these tumbling rates are also not yet fully understood. The high uncertainty in current tumbling rate information illustrates the need for on board processing systems to have the ability to observe and detect target object's rotation rates real time.

There are a few different methods that are currently being examined to detumble space debris, both contact and contactless methods. A brush contact that is utilized with a grasping capture method was previously discussed. This detumbling method has a high risk of breakup due to the uncertainty in most debris object's shape and size. An antenna

or appendage that was unknown about the debris object could collide with this brush as it attempts to decrease the object's tumbling rate. This high risk of the creation of additional space debris is a major disadvantage to using this method [23].

Multiple different contactless detumbling techniques employ an ion beam, electromagnetics, or lasers. These methods can target a specific point on the debris object to slow its rotation without coming into contact with the target object. The ion beam detumbling method involves complex physics and requires a large amount of investigation before this method matures. Electromagnetic methods of detumbling use eddy currents which are induced by a magnetic field that is generated from a coil. The force generated by these eddy currents can "brake" the tumbling of the target object, however these coils must be placed extremely close to the target object which raises the same risk as a contact detumbling method [27].

The use of lasers is a more developed method that can be used with all types of capture methods. The two primary forces that lasers implement onto a tumbling object are from light pressure and ablation. Although photons are massless, they carry momentum that can be transferred to a target object. Additionally, laser ablation occurs when a laser melts the surface of a target object creating plasma which generates a very small amount of thrust. The method of detumbling via lasers has been well-researched and proven to be successful in simulations [27].

The use of a pulsed laser is selected for detumbling activities that are required during this mission. Both the axis around which a target object tumbles, and the mass of the target object impact the length of time required to detumble the target. A simulation was developed by a group of researchers at the University of Strathclyde which used a laser

model and a rotational motion control algorithm to investigate laser detumbling capabilities [29]. This simulation analyzed the detumbling method of laser ablation to an Envisat-like satellite. The results of this simulation concluded that it took less than 14 days to detumble an object with a starting angular rotation rate of 3.5 deg. per second down to a rate of less than 1 deg. per second. Additionally, the laser that was used in this analysis had 860 Watts of available power [29].

3.3 Final Active Debris Removal Selection

The final selection for this mission's ADR system uses one capture method, one detumbling method, and one removal method. This ADR system will be used throughout the remainder of the mission design. The highest ranked capture method was found to be the net capture method (Fig. 8). The two highest ranked removal methods were found to be chemical engines and low thrust chemical engines. Both removal systems could be integrated with the net capture method, however the low thrust chemical engine was selected in this study. The low thrust option allows for multiple smaller engines which can be configurated for the engine exhaust plumes to avoid the space tether. Additionally, the low thrust option provides a simpler control algorithm and a lower risk of the space tether breaking compared to a higher thrust chemical engine.

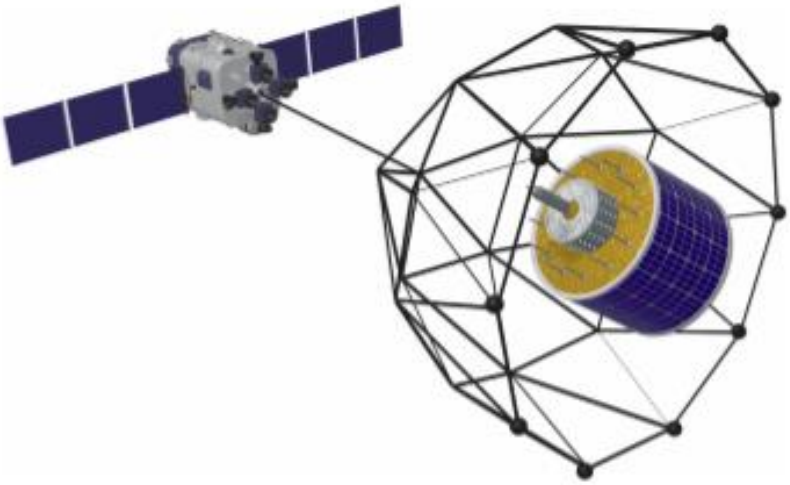

Figure 8: Net Capture Method Being Used on a Target Object [27].

The combination of a net capture system with a low thrust chemical engine removal method maintains a low risk while providing the capability to target a wide range of target types. Unlike many capture methods, the net capture method can target objects that have a low tumbling rate as well as targets with unique, or even unknown, vehicle configurations. The net capture method has also been shown to be a top candidate in ADR mission in a previous study which utilizes an AHP and utility-based comparison method [26]. Due to net capture displaying a high potential for ADR missions, net capture has been designed and used for multiple spacecraft missions [24][33].

The net capture system configurations have been investigated by many different researchers. Different net configurations and net capture technology have been extensively tested and analyzed to understand the mechanics of a net capture system. The net capture system can be modeled as a mass-spring model (Fig. 9). The results of this study specified the optimal net configurations, the closing mechanism on the net, and the potential to capture larger, tumbling target objects [25]. A hybrid tension control technique has

additionally been explored to find the control characteristics that are needed in tethered mission scenario [34]. The shape of space tethers has even been investigated to find optimal design characteristics for a future mission [7].

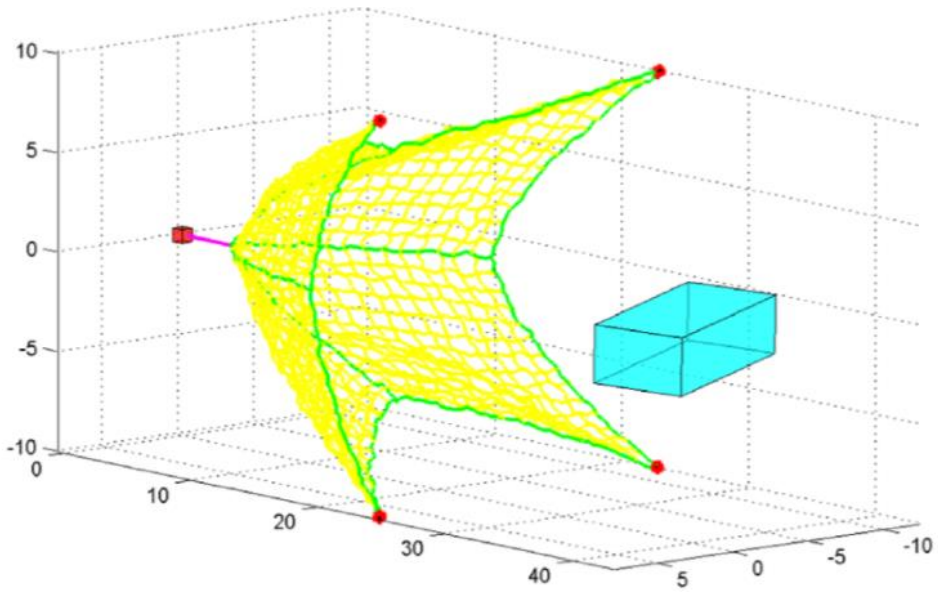

Figure 9: Numerical Simulation of the Net Capture Method. The net capture method was modeled as a mass-spring system to deploy onto a target [25].

The laser ablation method was selected to be used for detumbling capabilities. The capabilities of using a laser ablation were found to detumble an Envisat-like satellite from approximately 3.5 deg. per second to under a single deg. per second [29]. Therefore, this mission will provide a 10-day timeframe that will be used to inspect and detumble each given target object. This timeframe will provide designated mission time to reduce the tumbling of a target object as well as create a small buffer if the target object's tumbling rate is detected to be higher than expected. If tumbling detection capabilities further increase in the future, the necessity of a detumbling system may be eradicated since the net capture method can capture target objects with a low tumbling rate.

The selection of the ADR system is a net capture device that uses a low thrust chemical engine capability to reduce the targeted debris' altitude. Laser ablation will be used to reduce the tumbling rate of the target objects to successfully perform net capture. Net capture methods have been shown in numerical simulations to successfully capture a smaller object rotating at up to 5 deg. per second, although a lower tumbling rate will be required in this mission due to the large mass of the target objects. Additionally, creating a slight tension in the space tether using the low thrust chemical engines, as well as the low thrust used during the removal maneuver, should guarantee that the space tether will not break [25]. Furthermore, the low thrust chemical engine removal method could provide future capability of performing a controlled re-entry into the South Pacific Ocean Uninhabited Area (SPOUA).

Chapter 4

Debris Rendezvous Analysis

An analysis of the orbital mechanics of this mission is crucial for determining the mission architecture. These mission architectures utilize the launch of a "chaser" satellite, or satellites, into an initial orbit that will then rendezvous with the target objects. The chaser satellite will then detumble the target, if necessary, and execute the net capture. Once a target has been captured, it will be deorbited via a low thrust chemical engine system.

Different mission architectures were evaluated in terms of the mission timeline, delta-v requirements, and its capabilities to integrate with a desired launch vehicle. The mission architectures were initially analyzed using lower fidelity calculations, via MATLAB, until a final mission architecture was selected. The final mission architecture was then evaluated at a higher fidelity, using Ansys Government Initiatives' (AGI) System Tool Kit (STK), to obtain a more accurate depiction of the results.

A similar analysis method was used in a subsequent section to evaluate the deorbit portion of the mission. A lower fidelity calculation, using NASA's Debris Assessment Software (DAS), was used to identify initial deorbit delta-v values. Once these initial values were identified, a higher fidelity method, using AGI's STK, was used to calculate the results.

This analysis is used to provide approximate positions, timelines, and delta-v's for different mission architectures for both the rendezvous and deorbit portions of the mission. The sections written before each analysis act to clearly explain all assumptions that were made and to describe the setup and methodology that was used. This is important to understand the conditions in which the results apply to.

4.1 Rendezvous Analysis Methodology

Different assumptions were used to initialize the rendezvous analysis. The purpose of this mission was to generate a plan that could be executed in a feasible timeframe. A typical timeline for this mission type, which was characterized as a small program, should take approximately 4.5-5 years from concept to on-orbit checkout [35]. On orbit checkout is completed when a set of requirements are fulfilled after deployment of particular space system. Using this timeline, the orbital analysis of the mission was set to use the year 2028 as the analysis period.

An additional assumption was made on the launch vehicle selection. There are many different launch vehicles that can be used for this mission, but for our analysis the SpaceX Falcon 9 launch vehicle was selected because of the low cost, high mission success rate, and launch capabilities. The cost of a Falcon 9 launch is currently priced around $67MM if using a new Falcon 9 or as low as $50MM if using a reused Falcon 9. Additionally, the price projection for future launches could reach a cost as low as $28MM [36]. A major advantage of this launch vehicle is the ability to contribute towards the minimization of the overall mission cost.

An initial orbit was specified after the selection of the launch vehicle. This analysis assumed that it would take advantage of the Falcon 9's launch capability into a Sun-synchronous orbit (SSO). A Sun-synchronous orbit is an orbit with a high inclination whose goal is to maintain a consistent orientation to the Sun. Utilizing this capability, the Falcon 9 can launch the chaser into a 98 deg. inclination orbit, which is very advantageous since the target objects are all inclined around 98 deg. A plane change maneuver, which is used to change either the inclination or the Right Ascension of the Ascending Node (RAAN or Ω), is one of the most expensive maneuvers in LEO. The ability to launch into an orbit with a very similar inclination potentially reduces the cost of a large plane change. Choosing this launch vehicle with the SSO launch capability, the initial state of the chaser satellite was selected to be at an altitude of 300 km with an inclination of 98 deg. A launch timing method will be introduced in a subsequent section that will specify the RAAN initialization for the individual chasers.

The payload size for the Falcon 9 was used to develop maximum dimension and mass requirements for the chaser. Given the payload size of the Flacon 9 and its mass to orbit capability, the maximum characteristics of the chaser are 5.2 m in diameter, 13 m in length, and 22,800 kg in mass. Given this total mass, a dry mass estimate was found to be very helpful in the preliminary analyses. The dry mass of a system refers to the total mass minus the propellant mass. An average dry mass percentage of 73% was found to be a good initial estimate for a LEO mission [35]. Using this dry mass percentage estimate, and the maximum allowable mass for the Falcon 9 payload as a baseline, a dry mass maximum of 16,000 kg was initially assumed for the chaser satellite.

4.1.1 Low Fidelity Analysis

An initial analysis of the orbital maneuvers that are necessary for the rendezvous portion for each of the mission architectures was calculated using MATLAB. The primary function in this script is the calculation for a Hohmann transfer with a plane change. A Hohmann transfer calculates the optimal maneuvers for a transfer between two circular orbits that are in the same plane via an elliptical trajectory called the transfer ellipse. The Hohmann transfer requires two impulsive maneuvers to achieve this transfer, one at the transfer ellipse's periapsis and one at the transfer ellipse's apoapsis, where periapsis refers to the point in the orbit that is closest to the Earth and apoapsis refers to the point in the orbit that is furthest from Earth. The two maneuvers are calculated using the following equations,

$$\Delta v_1 = v_{t1} - v_{c1} = \sqrt{\frac{2\mu}{r_1} - \frac{\mu}{a_t}} - \sqrt{\frac{\mu}{r_1}} \tag{1}$$

$$\Delta v_2 = v_{c2} - v_{t2} = \sqrt{\frac{\mu}{r_2}} - \sqrt{\frac{2\mu}{r_2} - \frac{\mu}{a_t}} \tag{2}$$

where a_t is the semi-major axis of the transfer ellipse, μ is the gravitational parameter of Earth (3.986×10^5 km^3/s^2), r_1 is the radius of the initial circular orbit, and r_2 is the radius of the final circular orbit. The semi-major axis of the transfer ellipse is a useful metric which describes the longest radius of an ellipse. Additionally, the gravitational parameter is a constant used for calculations that involve Earth's gravity.

The plane change is calculated using the following equation [35],

$$\Delta v = 2v \sin\left(\frac{\Delta i}{2}\right) \tag{3}$$

where v is the velocity and Δi is the change in the inclination. The above equation calculates the plane change for a change in inclination. The change in RAAN can also be computed by switching the Δi term for a $\Delta\Omega$ term.

These two calculations can be combined to create a Hohmann transfer with a plane change equation. Since the plane change is directly related to the velocity of the orbit, the Hohmann transfer with plane change will execute the plane change at the apoapsis of the transfer ellipse. This guarantees that the lowest value of velocity will be used in the plane change equation. This is important to minimize the cost of the plane change maneuver. Therefore, the two changes in velocity that are required for a Hohmann transfer with a plane change going from an initial orbit in the outward direction is [35],

$$\Delta v_1 = v_{\mathrm{t1}} - v_{\mathrm{c1}} \tag{4}$$

$$\Delta v_2 = \sqrt{v_{\mathrm{t2}}^2 + v_{\mathrm{c2}}^2 - 2v_{\mathrm{c2}}v_{\mathrm{t2}}\cos(\Delta i)} \tag{5}$$

where v_{t1} is the velocity of the transfer ellipse at periapsis, v_{t2} is the velocity of the transfer ellipse at apoapsis, v_{c1} is the velocity of the initial orbit, v_{c2} is the velocity of the final orbit, and Δi is the change in inclination between the initial and final orbits. These

equations can also be used if going in the inward direction such as going from a higher orbit to a lower orbit, but the plane change must be applied at the first burn since the first burn would be at the apoapsis of the transfer ellipse.

This Hohmann transfer with plane change function was written into a MATLAB script. This MATLAB script, called the Hohmann Transfer with Plane Change (HPC) script, allows each rendezvous architecture to be modeled using a series of sequential transfers using the Hohmann transfer with plane change equations (Eqns. 4 and 5). The results of this script provide delta-v values for each maneuver. These values can be combined to provide a total mission delta-v or the total delta-v that is required for a chaser satellite.

To use the HPC script, it is initially assumed that both the chaser satellite and the target object are in a circular orbit. Since the target object's orbits have slight eccentricities, the script defines each target object's circular radius to be its average radius. This average radius was calculated by taking the average of the perigee and apogee values of each target object in Table 3. Additionally, it is necessary to assume that the maneuvers are impulsive and that the entire plane change is occurring at the apoapsis of the transfer ellipse. This assumption is used for simplicity, but a more optimal plane change would be split between the apoapsis burn and the periapsis burn with the larger portion being executed at apoapsis.

The mass of the propellant can be estimated after these delta-v's are calculated. The equation that is used to estimate the propellant mass is derived from the fundamental rocket equation [35],

$$m_{\text{prop}} = m_{\text{f}} \exp\left(\left(\frac{\Delta v_{\text{tot}}}{I_{\text{sp}} * g_{\text{o}}}\right) - 1\right) \tag{6}$$

where m_{prop} is the propellant mass, m_{f} is the final mass or dry mass (16,000 kg using SMAD mass estimates and the Falcon 9 payload size), Δv_{tot} is the total delta-v (provided by the above script), I_{sp} is the specific impulse of the engine (325 s for a typical impulsive chemical engine), which is an important engine characteristic, and g_{o} is the Earth's gravitational constant (9.8 m/s^2). This estimate is used to compare the propellant mass to the maximum payload mass that the launch vehicle can support to estimate the feasibility of each mission architecture.

4.1.2 High Fidelity Analysis

A higher fidelity analysis was conducted using AGI's STK software. This analysis is used for the first rendezvous architecture to check the similarity between the STK results and the aforementioned results obtained from the HPC script. This served as a Verification and Validation (V&V) test for the HPC script. Additionally, STK was used on the selected rendezvous architecture to get higher fidelity results.

The STK software is used for the higher fidelity analysis for several reasons. A primary reason is STK's ability to solve Lambert's problem, which is explained in Section 4.1.2.1, and to utilize a "Lambert Targeter" to calculate the maneuvers and timing for the rendezvous of a chaser satellite to a target object. Additionally, STK has the capability to use numerical solvers to propagate space objects through time in the existence of many different perturbations that can be specified by the user. The primary tool that is used within STK is Astrogator, a specific tool that allows for the design of a "mission control sequence" to design orbital maneuvers and trajectories for a specified object in STK. Additionally, a

target sequence can be constructed within a mission control sequence which allows for a specified computation to assist with the trajectory design.

4.1.2.1 Lambert's Problem

Lambert's problem uses the initial and final positions of the object and the time of flight between these positions to calculate the trajectory between the two positions. There is a well-defined solution to Lambert's problem, and there are many different solution methods that have been developed since the development of this problem. There are a variety of ways to solve Lambert's problem even within STK.

For this analysis, the Lambert Search Profile was used during a target sequence within Astrogator. The Lambert Search Profile is an option for trajectory design within a target sequence that identifies the optimal transfer, in terms of lowest delta-v, between two different positions in space. One primary nuance to this trajectory design tool is that it only considers two body gravitational effects. The specifics of a two-body gravitational model will be described shortly. The Lambert Search Profile calculates four primary values: the initial wait time until the first maneuver, the first maneuver thrust vector, the transfer time between the two maneuvers, and the final maneuver thrust vector.

STK searches over a range of possible solutions to converge on an optimal solution using a solution method called a cosine transformation [37]. The cosine transformation can be explained by first reviewing the Gauss problem. The Gauss problem develops Lagrange functions that can be used to find the final position and velocity vectors given an initial position and velocity vector of a desired orbital object [38],

$$\overrightarrow{r_2} = f\overrightarrow{r_1} + g\overrightarrow{v_1} \tag{7}$$

$$\overrightarrow{v_2} = \dot{f}\overrightarrow{r_1} + \dot{g}\overrightarrow{v_1} \tag{8}$$

where f, g are Lagrange functions, and $\dot{f}$ and $\dot{g}$ are their derivatives with respect to time, that solve for a final position and velocity given an initial position and velocity. The Lagrange functions and their derivatives can be expressed in terms of eccentric anomaly (E), which is used to describe the position along the transfer ellipse, such that [38],

$$f = 1 - \frac{a}{r_1}(1 - \cos \Delta \mathrm{E}) \tag{9}$$

$$g = t - \sqrt{\frac{a^3}{\mu}}(\Delta E - \sin \Delta E) \tag{10}$$

$$\dot{f} = \frac{-\sqrt{\mu a}}{r_1 r_2} \sin \Delta E \tag{11}$$

$$\dot{g} = 1 - \frac{a}{r_2}(1 - \cos \Delta \mathrm{E}) \tag{12}$$

where r_1 is the initial orbit radius, r_2 is the final orbit radius, a is the semimajor axis of the transfer ellipse, t is the time of flight, and ΔE is the change in eccentric anomaly.

This method (Gauss' Method) was restricted to only elliptic transfers, so a set of universal variables were developed so that it could be defined for all conic orbits. The

universal variables, x and z, were developed and after further derivation, can be used to simplify the Lagrange functions and their derivatives to the following equations [38],

$$f = 1 - \frac{x^2}{r_1} C \tag{13}$$

$$g = t - \frac{x^3}{\sqrt{\mu}} S \tag{14}$$

$$\dot{f} = \frac{-\sqrt{\mu}}{r_1 r_2} x(1 - zS) \tag{15}$$

$$\dot{g} = 1 - \frac{x^2}{r_2} C \tag{16}$$

where x and z are universal variables, and C and S are functions of the universal variable z that allow for a power series expansion to be used as z approaches zero. This set of Lagrange functions can now be used to solve a transfer trajectory of any conic orbit including hyperbolic, elliptic, and parabolic trajectories [38].

The cosine transformation method follows a similar derivation and takes advantage of the relationship between the universal variables and the eccentric anomaly. It additionally uses a relationship with the hyperbolic anomaly (F) to allow for a more diverse set of solution trajectories,

$$\frac{x}{\sqrt{a}} = \Delta E, \qquad \frac{x}{\sqrt{-a}} = \Delta \mathrm{F}, \qquad z = q^2 \tag{17}$$

where x and z are universal variables, a is the semimajor axis of the transfer trajectory, q is a new variable which relates to the universal variable z, and E and F are the eccentric and hyperbolic anomalies.

The cosine transformation then introduces a new universal iterate variable, k, which is dependent on the eccentric anomaly,

$$\cos(\Delta E) = k^2 - 1 \tag{18}$$

This relationship is applied to the equations in Eqn. 17 to combine the derivation of the TOF equation with the new iterate variable k. This new variable k is used to iterate the TOF equation to search for different solutions. The final time of flight equation which can be iterated to solve for a transfer trajectory was found to be,

$$\mathrm{TOF} = S\sqrt{1 - k\tau}\left[\tau + (1 - k\tau)\left(\frac{q}{\sqrt{(2 - k^2)^3}} - \frac{k}{2 - k^2}\right)\right] \tag{19}$$

where S and τ are geometry variables, q is equal to $\sqrt{z}$, and k is the universal iterate variable [39]. A more in-depth derivation and implementation details including initial guess generation can be found in Ref. 39.

4.1.2.2 Propagators

Propagators use different numerical integrators to iteratively apply desired perturbations to a target object as it advances through time. There are many different propagators that can be used by default within STK that incorporate different orbital perturbations. An additional feature that STK provides is the capability to build a customized propagator to include user defined perturbations.

The Earth Point Mass propagator was used during the rendezvous portions of this analysis. This propagator only considers the two body gravitational effects between the Earth and the chaser satellite. This gravitational model only incorporates the masses of the objects and their distance apart from each other. A 7^{th} order Runge-Kutta-Fehlberg integrator, which is the default integrator within STK, is used for the numerical integrator for this propagation selection. This integrator provides the numerical solutions to the ordinary differential equations that are required for the propagation model [37].

The propagator that is used with the target objects is called the Simplified General Perturbations (SGP4) Propagator. The target objects are inserted into STK via a two-line element set (TLE) file on December 7, 2022, which describes the object's orbital characteristics at a particular point in time. STK provides the option to automatically update the TLE which can update the newest version of these orbital characteristics, but this option was turned off to maintain consistency during the analysis. The SGP4 propagator primarily considers the following perturbations: atmospheric drag, third body effects of the Sun and Moon, and Earth oblateness effects.

The atmospheric drag solves for the force that the atmospheric particles have on the surface of the satellite. Third body effects of the Sun and Moon utilize an additional

gravitational body into the computation. These third body effects assume that the Sun and Moon are point masses and only consider the gravitational force that they exert on the satellite given the distance and mass relationship. The Earth oblateness effects create a non-uniform gravitational force model due to the non-spherical shape of the Earth which create additional forces to a body that is in orbit.

A new propagator was designed to compute longer propagation segments for the chaser object more accurately than the two-body gravitational model. Figure 10 shows the different perturbations and their acceleration contribution at different distances from Earth. This mission analysis will primarily be located around and beneath the first dotted line (approximately 780 km altitude). This new propagator will only include perturbations that will affect the acceleration of the object on the order of 10^{-10} km/s and above. This region can be found in the highlighted area on Figure 9. The perturbations that are located within this region are: gravitational effects up until at least the 18^{th} order which indicate the accuracy of the spherical harmonics that model Earth's gravitational field, third body effects from the Sun and the Moon, dynamic solid tides which is a geopotential perturbation, and atmospheric drag [40].

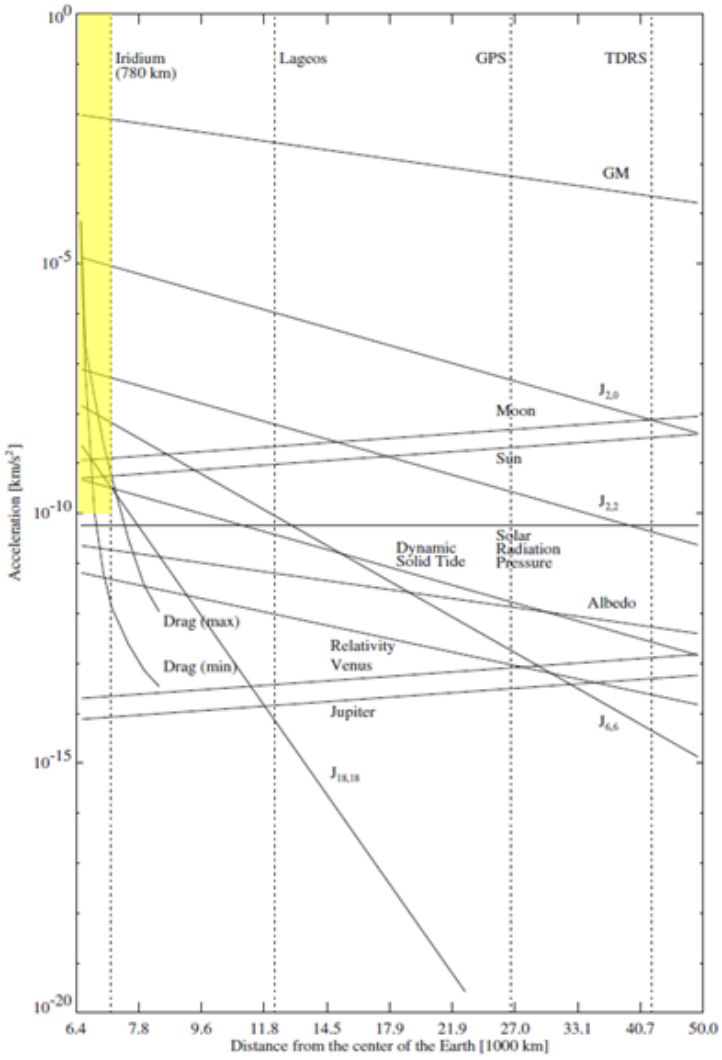

Figure 10: Acceleration Effects of Different Orbital Perturbations. This study focuses on perturbations in the highlighted region [40].

Using these perturbations as a guide, the new propagator was developed. This propagator uses a 21 x 21 gravitational force model. The 21 x 21 model specifies the accuracy of the spherical harmonics that are used to model the Earth's surface. Additionally, the gravitational model incorporated the permanent solid tides which account for the surface displacement of Earth because of gravitational effects of the Sun and Moon. The drag model of the chaser satellite is assumed to be spherical and is calculated with a

Jacchia-Roberts atmospheric density model which is a state-of-the-art atmospheric density model. A file was uploaded to the drag model which contained current predictions of the F10.7, which is a measurement of the solar cycle intensity, since the solar cycle has been found to substantially impact the acceleration due to drag [41]. The solar cycle is a phenomenon in which the Sun's magnetic field flips inducing increased solar activity which increases the effects of atmospheric drag. Additionally, the third body effects are included for the Sun and the Moon. This propagator was selected to use the 7^{th} order Runge-Kutta-Fehlberg integrator to compute the numerical integration required by applying these different orbital perturbations.

An important note is that since this mission is being analyzed to rendezvous with target objects in 2028 using the SGP4 propagator with an initial TLE from 2022, there will be high levels of error in the position of these target objects. Additionally, the atmospheric density models that are being used for this analysis are being estimated out to 2028 which could be different compared to the actual atmospheric density model that will be present in 2028. It is necessary to remember that there are inherent errors in these propagators, but they should still produce approximate values that can be very useful in future analyses. These errors can be minimized in future studies by using high fidelity propagators or by rerunning these calculations closer to the mission, minimizing long term propagation errors.

4.1.2.3 Engines

Different engines can be designed for use in STK Astrogator's maneuver segments. All maneuvers during this analysis are estimated to have low burn times, so to simplify

computations all the maneuvers will assume to be an impulsive burn. A user specified engine was designed to be used for the rendezvous portion of this analysis. Different bipropellant rocket systems were compared, and the selected engine was the TR-312-100MN Dual Mode Liquid Apogee Engine [35].

The nominal thrust of this engine is listed to be 503 N with a specific impulse (I_{sp}) of 325 seconds. These values were ingested into the new STK engine design. The mass and length of the engine are listed as 6.03 kg and 0.71 m, respectively. Additionally, the propellant that is used in this engine is Dinitrogen Tetroxide (NTO) and Monomethylhydrazine (MMH) [35]. These characteristics can be used if further design is required in subsequent sections.

4.1.3 Nodal Precession

The primary perturbations that are found in LEO can affect orbits in many ways. The Earth's oblateness, J_2 perturbation, influences the Keplerian orbital elements, RAAN (Ω) and Argument of Perigee (ω). Nodal precession ($\dot{\Omega}$), also called RAAN drift, is a phenomenon in which the RAAN drifts eastward over time due to non-uniformities in the spherical harmonic gravity field model. The precession of perigee ($\dot{\omega}$) works similarly with the Argument of Perigee although it typically precesses in the opposite direction. These drift rates can be calculated using the following formulas [38],

$$\dot{\Omega} = -\frac{3nJ_2R_{\text{Earth}}^2}{2a^2(1-e^2)^2}\cos(i) \tag{20}$$

$$\dot{\omega} = -\frac{3nJ_2R_{\text{Earth}}^2}{2a^2(1-e^2)^2}\left(\frac{5}{2}\sin^2(i) - 2\right) \tag{21}$$

where n is the mean motion, J_2 is a constant that describes the oblateness of the Earth, R_{Earth} is the radius of the Earth, a is the semimajor axis of the orbit, e is the eccentricity of the orbit, and i is the inclination of the orbit.

This nodal precession can be advantageous to a multi-target rendezvous mission and has been previously investigated to be used in different ADR mission architectures [42]. If a chaser satellite is placed in a higher orbit than the target object's orbit, the RAAN precession can change the chaser's orbital plane naturally compared to the target object. This feature has the potential to save from expensive plane change maneuvers as well as to save an entire launch if multiple target objects can be targeted by a single chaser. Nodal precession could influence many of the rendezvous mission architectures to utilize this "free" delta-v.

An initial study was investigated via MATLAB to check the feasibility of using nodal precession with the previously selected target objects. A relationship between delta-v and difference in precession rate would give insight to the amount of delta-v required to raise the chaser to a high enough altitude to achieve a difference in precession rate that could drift between two selected target objects.

For this study, the target object is assumed to be Envisat to provide a target object's altitude. The delta-v's required to execute a Hohmann transfer from this target's altitude to different "raised" altitudes were calculated. Additionally, Eqn. 20 noted above for the nodal precession rate was calculated at both the target and raised altitudes. The differences

between these two rates were recorded. This would be the drift rate that the chaser would have relative to the target object (Fig. 11).

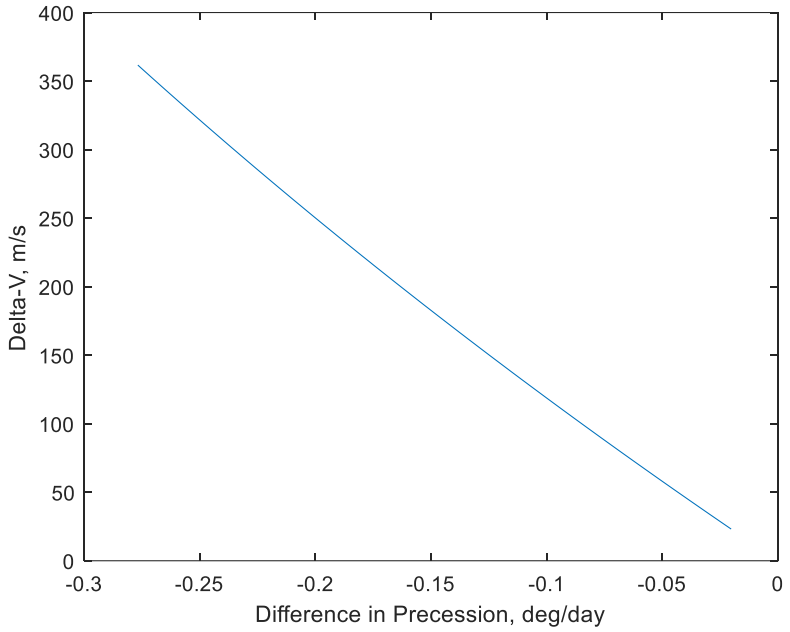

Figure 11: Difference in Precession Rate for Different Delta-Vs. A near-linear relationship was found between the delta-v cost to raise the spacecraft's orbit and the difference in precession between the target and raised orbit.

The results of this study show that there was a near-linear relationship between the difference in precession rate and the delta-v's required to raise the chaser to a raised orbit. This delta-v was only calculated for the chaser to get to the raised orbit. A similar delta-v cost can be assumed for the journey back down to a similar target orbit once the RAAN aligned with a new target object. A raised orbit of 1,400 km was chosen to continue this study. The delta-v required to reach this raised orbit was approximately 300 m/s. The difference in precession rate between the target object's orbit and the chosen raised orbit is approximately -0.25 deg./day.

The target objects orbital elements were taken from STK to see the differences in their RAANs using a report that find the target object's Keplerian orbital elements for

January 1, 2028, at 00:00:00.000 UTCG (Table 11). The RAANs for the different target objects range from approximately 27 deg. to 310 deg. The large difference between all of these target objects would likely take a long time to use this natural plane change to target all five objects. However, some of the target objects do have similar RAANs. The first target object (Envisat) and the third target object (H-2A RB) have less than a 2 deg. difference between their respective RAANs. A visualization of the different RAAN values among all of the target objects can be seen using STK (Fig. 12).

Table 11: Target Object's Keplerian Orbital Elements on Jan. 1, 2028. The highlighted column displays the RAAN values for each of the target objects.

Target Object	a (km)	e	i (deg.)	Ω (deg.)	ω (deg.)	ν (deg.)	M (deg.)
Envisat	7133.721	0.001753	98.054	283.435	119.707	184.093	184.107
ADEOS	7165.614	0.001104	99.093	86.817	46.558	86.558	86.431
H-2A RB	7159.969	0.00677	98.027	285.322	354.154	332.684	333.038
ADEOS-II	7164.830	0.000693	98.511	310.507	346.709	122.773	122.706
Ariane 5 RB	7150.348	0.001894	98.805	27.156	254.985	132.782	132.622

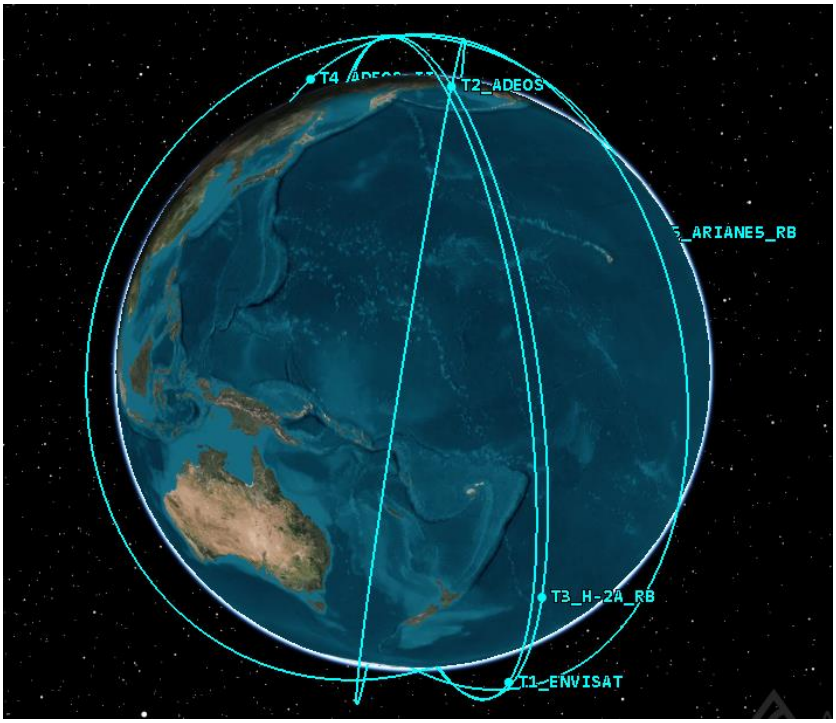

Figure 12: STK Visualization of the RAAN Separation of the Target Objects.

The usage of nodal precession for at least some of the selected set of target objects is shown to be feasible. The subsequent rendezvous mission architectures will provide a more in-depth analysis of the application of this phenomenon. A conclusion to this nodal precession study suggests that a set of target objects could be chosen to further take advantage of nodal precession such as choosing a set of target objects with similar RAANs. Additionally, if the target objects were located in a more equatorial orbit, they would experience higher precession rates (Fig. 13). This could possibly lead to higher differences in precession rates at a lower delta-v cost.

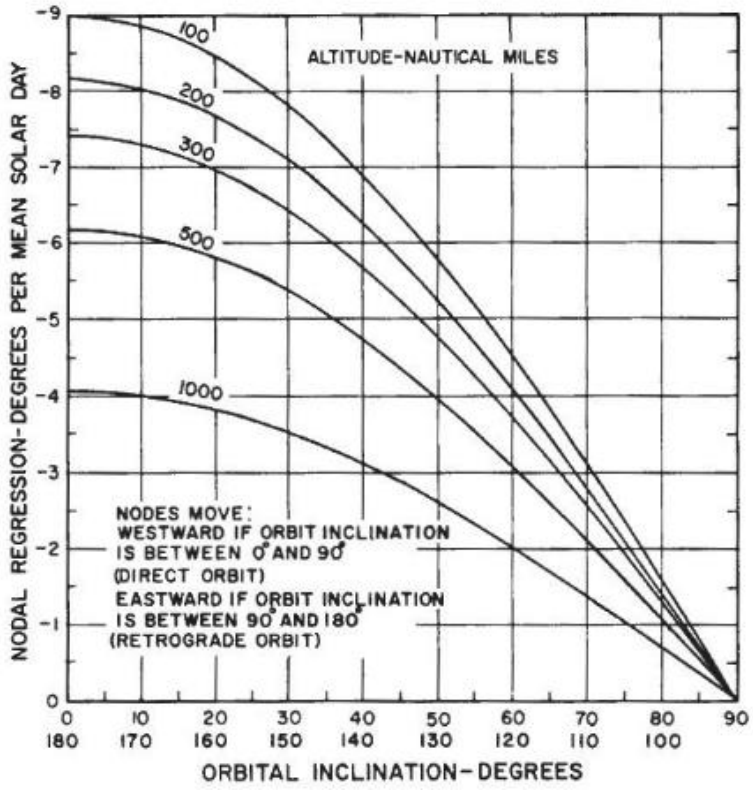

Figure 13: Nodal Regression Rates as a Function of Inclination and Altitude. Notice, the more equatorial and lower the orbit of a spacecraft, the higher the nodal precession rate is found to be [38].

4.1.4 Launch

The last initial condition that needs to be discussed is how the launch and launch timing was modeled. The launch was modeled by placing the chaser satellite in its initial orbit, 300 km, with a RAAN value that is aligned with the Vandenberg Air Force Base. This launch location was selected because it is typically used for launching payloads into a SSO. Using this launch location, an assumption was made that the chaser will be launched into a 98 deg. circular orbit with its orbital plane aligned overtop the Vandenberg Air Force Base.

The launch timing would give an initial date and time that was needed to find the day that the rendezvous would begin on. As a result of the previously discussed nodal precession, the target object's RAANs continually regress as time passes. The most fuel-efficient rendezvous trajectory would occur when the orbital planes aligned which would minimize the usage of a plane change maneuver. Therefore, the primary use of the launch timing is to provide a start day to solve the Lambert Search Profile which can then find the optimal transfer trajectory given a specified window.

Using STK, accesses were computed between Vandenberg Air Force Base and the target objects. Accesses are used in STK to find line-of-sight between designated objects. A 2 deg. from the vertical constraint was used on the access to model when the target object would pass overtop the launch location. The first accesses that occurred in 2028 with the previously stated constraints were computed. The accesses were checked to verify that the motion of the target objects was ascending, as opposed to descending which would be a 180 deg. offset from the desired RAAN. After these accesses were computed, the day was recorded for use in the Lambert Search Profile and the RAANs were recorded to be used for the initial state of the chaser (Table 12).

Table 12: Rendezvous Day with corresponding first access with Vandenberg AFB, the rendezvous day, and the RAAN values for each target object.

Target	First Access	Rendezvous Day	RAAN
1	15 Jan 2028 19:52:54.464	15 January	297.605
2	27 Jan 2028 06:50:08.019	27 January	113.796
3	8 Feb 2028 19:54:28.664	8 February	321.996
4	15 Jan 2028 21:41:41.208	15 January	325.226
5	2 Jan 2028 02:46:44.505	2 January	28.287

4.2 Mission Architecture 1

The first mission architecture will be the simplest scenario. This architecture will contain five separate launch vehicles that will individually launch the chaser satellite in its initial orbit. The chaser will then rendezvous with its corresponding target object, perform a laser detumble if necessary, and then execute the net capture. Once the chaser has captured the target object, it will deorbit both itself and the target object. The sequence is then repeated for each of the chaser satellites (Fig. 14).

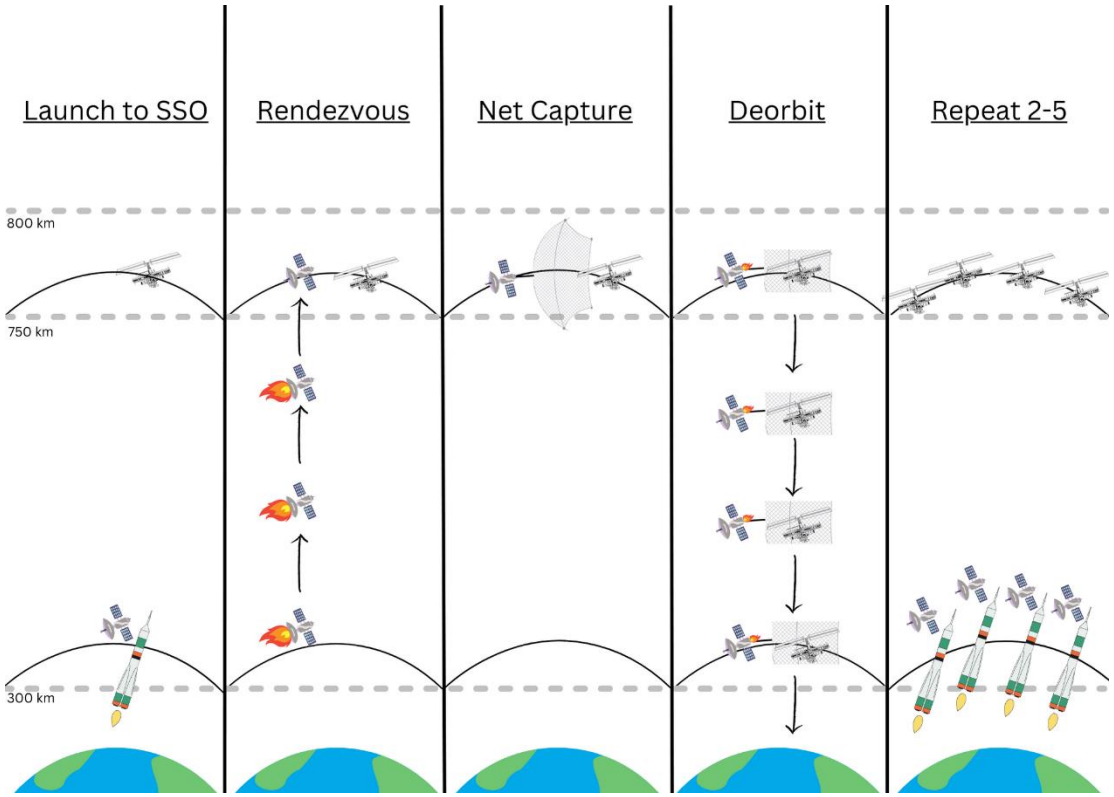

Figure 14: Mission Architecture 1. This mission architecture is composed of five separate launch vehicles each carrying a chaser that then directly rendezvous with the five target objects.

Initial delta-v calculations were found based on the previously discussed lower fidelity analysis (HPC script). The delta-v required to achieve the initial orbit was not calculated. The Hohmann Transfer with plane change function was used to move the chaser satellite from its initial orbit to the orbit of a target object. The results of all five launches rendezvousing with each of the five target objects are shown in Table 13. The largest total delta-v is 313.72 m/s, from Chaser 2, while the least expensive rendezvous maneuver is 257.97 m/s from Chaser 1. The primary differences between required delta-v values come from the slight differences that the target objects have in terms of semimajor axis, eccentricity, and inclination.

Table 13: Mission Architecture 1 Low Fidelity Analysis Results. Each launch is found to have a total delta-v requirement between approximately 250 and 315 m/s.

Launch	DV 1 (m/s)	DV 2 (m/s)	Total DV (m/s)
1	128.75	129.22	257.97
2	136.43	177.28	313.72
3	134.05	133.76	267.81
4	138.02	157.35	295.37
5	130.74	150.09	280.83
Total	667.99	747.70	1415.70

An STK analysis was run for this rendezvous architecture to compare results with the HPC script. This section of the analysis utilizes the previously discussed Lambert's Problem in the form of STK Astrogator's Lambert Search Profile. The initial conditions given to each of the chaser satellites were a 300 km periapsis altitude, a 300 km apoapsis altitude, their respective RAAN values given in Table 12, and an initial orbit epoch of their respective rendezvous day set at 00:00:00.000 UTC. Additionally, the spacecraft parameters were changed to set the dry mass to equal 16,000 kg, the dry mass assumption that was made previously, to generate more accurate fuel estimates.

A mission control sequence (MCS) was established for each of the chaser satellites. Figure 15 shows the mission control segments and the order that they were used. The segments within the Target Sequence are being solved via the Lambert Search Profile. The first Propagate within the Target Sequence will contain the wait time that is needed for an efficient transfer. The Maneuver segment will contain the thrust vector for the first burn.

The Propogate1 segment contains the time of flight of the transfer arc, and the Maneuver1 segment is the final burn thrust vector.

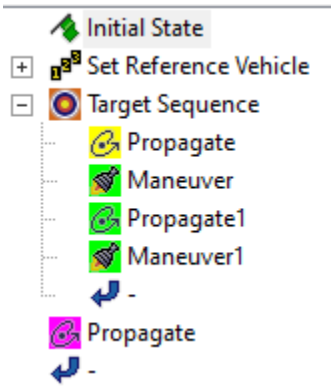

Figure 15: Mission Architecture 1 Astrogator Mission Control Sequence.

The Set Reference Vehicle segment is used to initialize the chaser's target object so that the Radial, In-Track, Cross-Track (RIC) frame can be used. The three vectors in the RIC frame are in the direction of the radius vector (Radial), the orbit plane normal (Cross-Track), and the along track vector (In-Track). Within the Lambert Search Profile set-up, the RIC frame relative positions and velocities relative to each chaser's target object are set to zero to design for rendezvous. In practice, the chaser would need to establish a target offset in position, but for simplicity this analysis uses values of zero for both the relative position vector and relative velocity vector. Additionally, the Lambert Search Profile was not initialized to match the phase of the target object, but to only achieve the target objects orbital plane. This was decided due to the high error from the SGP4 propagator. A phase match with the target objects could be calculated in the future using a higher precision propagator, and the launch window could thus be adjusted.

The Lambert Search Profile utilizes a user-defined grid-search to find the optimal timing and maneuver. This analysis used a one-day investigation window with a five-

minute grid search time step. The propagate segments within the Target Sequence use the Earth Point Mass propagator. An Earth Point Mass propagator is assumed since the wait time and time of flight are both short intervals (less than a day each). These short propagation segments would result in very low perturbation accelerations if a higher fidelity propagator was used. Additionally, this assumption eradicated the need to use a differential corrector to adjust for perturbations since the Lambert Search Profile also assumes only two body gravitational effects, or Earth Point Mass propagation.

The final initialization of the Target Sequence was regarding the maneuver segments. The engine model was adjusted to use the TR-312-100MN Dual Mode Liquid Apogee Engine for an impulsive burn. Each of these maneuver segments contain a thrust vector that, after the Lambert Search Profile has been run, will represent one of the two burns needed to rendezvous with a target object. The first chaser was then assigned to the first target object, the second chaser was assigned to the second target object, and the remaining chasers continued this pattern to find their corresponding target object. The Lambert Search Profile was then executed and then values for the delta-v and the estimated fuel mass are given in Table 14.

Table 14: Mission Architecture 1 STK Results. Notice the similarity in results between this analysis and the lower fidelity analysis.

Chaser	Begin Maneuver	DV 1 (m/s)	DV 2 (m/s)	Total DV (m/s)	Total Est. Fuel (kg)
1	15 January	125.59	125.89	251.48	1276.57
2	27 January	155.71	146.91	302.62	1530.03
3	8 February	135.24	125.65	260.89	1323.34
4	15 January	139.85	135.91	275.75	1397.13
5	2 January	138.10	138.78	276.88	1402.73
Total	-	694.49	673.14	1367.62	6929.8

The delta-v values were found to agree very well with the lower fidelity analysis results. Both the minimum and maximum rendezvous delta-vs are with the same chasers. There is a slight reduction in all the STK results compared to the HPC script results. This difference is intuitive because STK solves for an optimal solution while the HPC script solves a single equation for a Hohmann Transfer with a plane change.

The fuel estimations for each chaser satellite were all found between approximately 1,200 kg and 1,600 kg with the assumption of a 16,000 kg chaser dry mass. The fuel estimations and the dry mass of the chaser were combined to find a total mass estimate of each chaser, between 17,200 kg and 17,600 kg. The total masses of the individual chaser satellites were found to be under the launch vehicle's maximum payload mass capability of 22,000 kg. This result led to the design of more complex mission architectures, which could lower the overall mission cost by maximizing the launch vehicle's payload capacity.

4.3 Mission Architecture 2

The second mission architecture that will be investigated is shown in Figure 16. A single launch vehicle will place the chaser into its initial orbit. The chaser used in this mission architecture will contain five deployable "deorbit kits", each containing a net capture system and a propulsion system to perform the deorbit maneuver. The chaser will rendezvous with the first target object and deploy a deorbit kit. The chaser will then raise its own orbit to 1400 km to wait to match the plane of the next target object utilizing nodal precession. Once the plane has matched, the chaser will decrease in altitude to rendezvous with the next target object where it will deploy a second deorbit kit. This sequence will

continue raising and lowering the chaser's orbit until all the deorbit kits have been deployed onto all of the target objects.

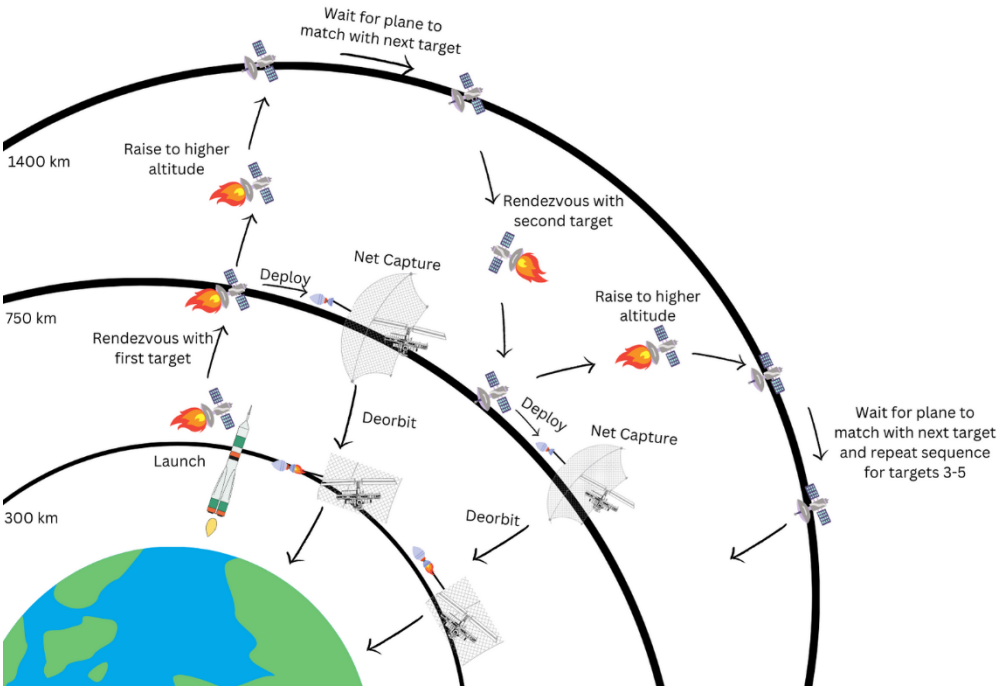

Figure 16: Mission Architecture 2. This mission architecture uses one launch vehicle with one chaser that rendezvous with all five target objects.

This mission has a variety of strengths compared to the first mission architecture. Taking advantage of nodal precession, this mission architecture could allow for the use of single chaser satellite to rendezvous with all five different target objects. Using a single chaser satellite would reduce total mission cost significantly since only one launch would be needed. A single chaser satellite manufacture would additionally reduce the cost by only requiring a single laser detumbling system and one set of solar panels.

The order that the target objects will be targeted is very important for this mission architecture. Target objects should be ordered by their RAAN values so that the most

efficient use of the nodal precession can be explored. Each target object and their corresponding RAAN value as calculated on January 1, 00:00:00.000 UTCG is reiterated in Table 15 as found from the results of the J2000 Classical Orbital Elements in Table 11.

Table 15: RAAN Values for Each Target Object calculated on January 1, 2028.

Target Number	Target Object	Ω (deg.)
1	Envisat	283.435
2	ADEOS	86.817
3	H-2A RB	285.322
4	ADEOS -II	310.507
5	Ariane 5 RB	27.156

The nodal precession rate at the chosen raised orbit is estimated to be -0.25 deg./day. This negative rate shows a natural regression in RAAN between the chaser at this raised orbit and the target objects. The order of the target objects was then selected from the largest RAAN value to the smallest RAAN value resulting in the following order: Target 4, Target 3, Target 1, Target 2, then Target 5. Using this ordering with the corresponding RAAN values, an initial wait time was computed to find the number of days required to naturally change planes between target objects.

The initial delta-vs and wait times were first computed using the HPC script. The delta-v values for rendezvous and for raising the chaser's orbit used the Hohmann Transfer with plane change function. The wait times were found using the -0.25 deg./day precession rate and the difference in RAAN between the targets. The results are found in Table 16.

Table 16: Mission Architecture 2 Low Fidelity Analysis Results. These results display the approximate time required to match the phase with the next target object and the delta-v values for the raise and rendezvous maneuvers.

Rendezvous	Target Number	ΔRAAN (deg.)	Approx. RAAN sync (days)	Raise Delta-v (m/s)	Rendezvous Delta-v (m/s)	Total Delta-v (m/s)
1	4	-	-	-	295.4	295.4
2	3	25.2	101	293.3	310.7	604.0
3	1	1.9	7.6	301.1	311.5	612.7
4	2	196.6	786.4	311.5	320.1	631.6
5	5	59.6	238.4	296.4	312.1	608.5
Total	-	283.3	1133.4	1202.3	1549.8	2752.2

This second mission architecture was found to have a total delta-v of approximately 2,752 m/s. A propellant mass check was used to check the feasibility of this mission architecture with our launch vehicle selection. Using Eqn. 6, the propellant mass required for this chaser satellite was estimated to be 21,966 kg assuming a 16,000 kg dry mass. The total mass of the chaser system would then be approximately 37,966 kg, which is far greater than the launch vehicle's payload limit of 22,000 kg. Additionally, the total wait time that would be required for the chaser in the raised orbit, referenced as RAAN sync time in the table, is approximately 1,133 days, which is significantly over the one year rendezvous goal.

This initial analysis suggested that the second mission architecture is not a feasible selection for many reasons. The total mass of the chaser system is estimated to be almost twice the launch vehicle's payload mass limit. Also, the total RAAN sync time is over three times the requirement to rendezvous with all the targets in less than one year. A single chaser cannot be used to rendezvous with this mission's set of target objects within the

mission requirements. However, a quick investigation into the different RAAN sync times, some of these times are low while others are very high, suggest that a different mission architecture could still be designed to take advantage of nodal precession while staying within the mission requirements by using a single chaser to target the target objects with similar RAAN values.

4.4 Mission Architecture 3

The third mission architecture attempts to take advantage of nodal precession while staying within the mission requirements (Fig. 17). Four launches will be used to rendezvous with the five target objects. The first launch will contain a single chaser that will rendezvous with the two target objects that are closest in RAAN values. The other three launches will each contain a single chaser that will independently rendezvous and deorbit with a single target object. A consequence of this mission architecture is that there would need to be two different chaser satellite designs which would add complexity to the overall mission. The chaser in the first launch would contain two deployable deorbit kits while in launches 2-4 the chaser would have both capture and deorbiting capabilities.

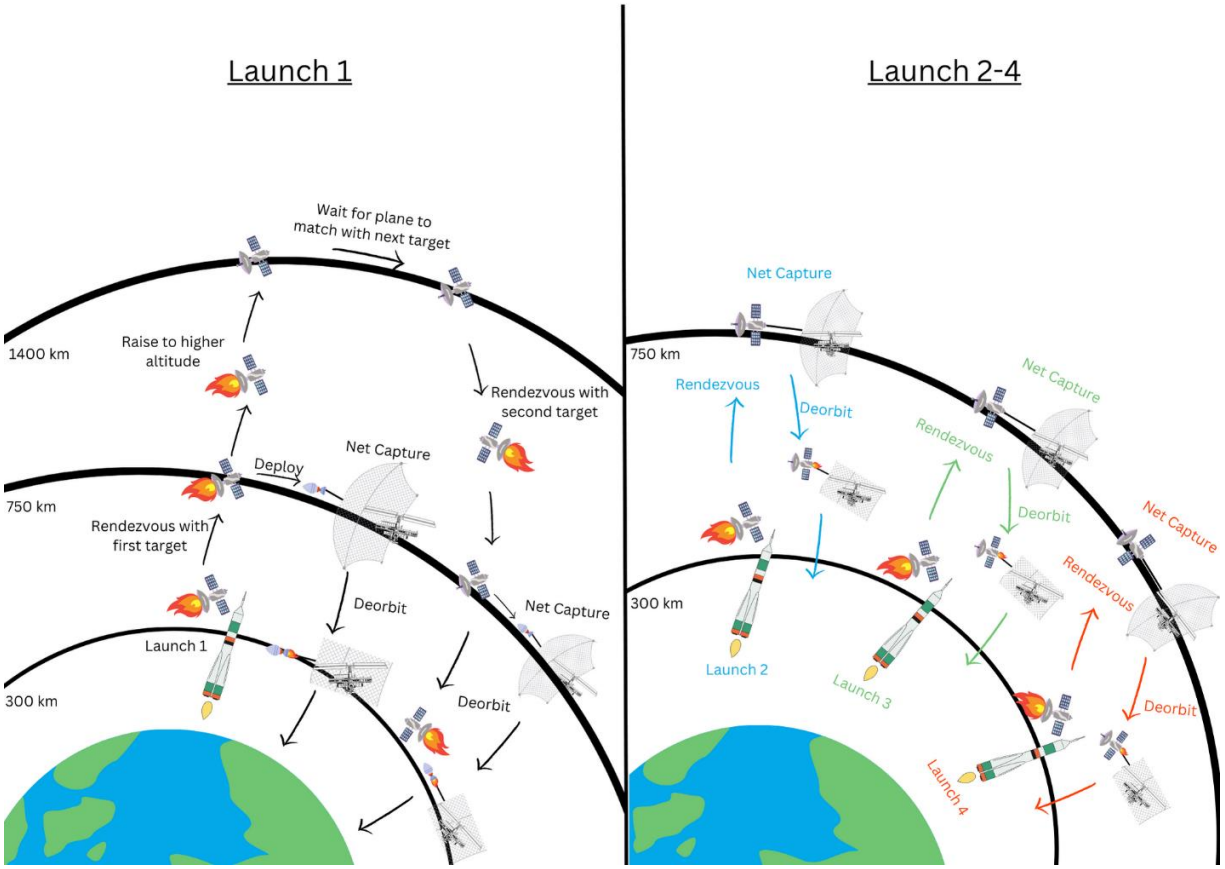

Figure 17: Mission Architecture 3. This mission architecture is composed of four separate launch vehicles each carrying a chaser. The first chaser is used to rendezvous with two target objects leveraging nodal precession, and the remaining three launch vehicles directly rendezvous with the three remaining target objects.

Choosing the two target objects that have the closest RAAN can be found from Table 15. Target 3 and Target 1 are separated by a 1.9 deg. difference in RAAN. Approximately 7.6 days is the RAAN sync time that would be required for the chaser to naturally change planes from the Target 3 to Target 1. Initial delta-v calculations were computed using MATLAB and the Hohmann Transfer with plane change function (Table 17).

Table 17: Mission Architecture 3 Low Fidelity Analysis Results. Notice the chaser used in Launch 1 utilized the nodal precession to rendezvous with two target objects, while the chasers in Launches 2-4 only had one target object.

Launch	Target Number	Raise Delta-v (m/s)	Rendezvous Delta-v (m/s)	Total Delta-v (m/s)
1	3	-	267.8	267.8
	1	301.1	311.5	612.6
2	2	-	313.7	313.7
3	4	-	295.4	295.4
4	5	-	280.8	280.8
Total	-	301.1	1469.2	1770.3

The first chaser was found to have a total delta-v of 880.4 m/s which could be much more feasible than the previous mission architecture's total delta-v 2,752.2 m/s. The propellant mass estimated for the first chaser was found to be 5,094.86 kg using Eqn. 6. This results in the chaser total mass to be approximately 21,094 kg and with a RAAN sync time of 7.6 days. This multi-target chaser thus satisfies the launch vehicle payload mass and mission requirements.

Although this mission architecture is feasible, launches 2-4 could be greatly improved. These launches are identical to the launches in mission architecture one which do not maximize the use of the launch vehicle's payload mass capability. Additionally, a RAAN sync time of 7.6 days and a total dry mass of 21,094 kg are both under requirements. Therefore, an additional mission architecture could be designed to take advantage of the mission requirements.

4.5 Mission Architecture 4

The fourth mission architecture takes advantage of nodal precession while attempting to maximize the use of the launch vehicle's payload mass capability of 22,000 kg. This mission architecture will use two launches to initialize two separate chaser satellites and is displayed in Figure 18. The target objects can be grouped by their differences in RAAN to provide a set of three target objects that are similar in RAAN, and a set of two of the remaining target objects. The first chaser will rendezvous with the set of two target objects while the second chaser will rendezvous with the set of three target objects. Both chasers will utilize nodal precession via the raised orbit and will use deployable deorbit kits that will capture and deorbit their respective target object. Additionally, this mission architecture would only require a single chaser design with the capability of deploying three deorbit kits which could reduce the mission complexity.

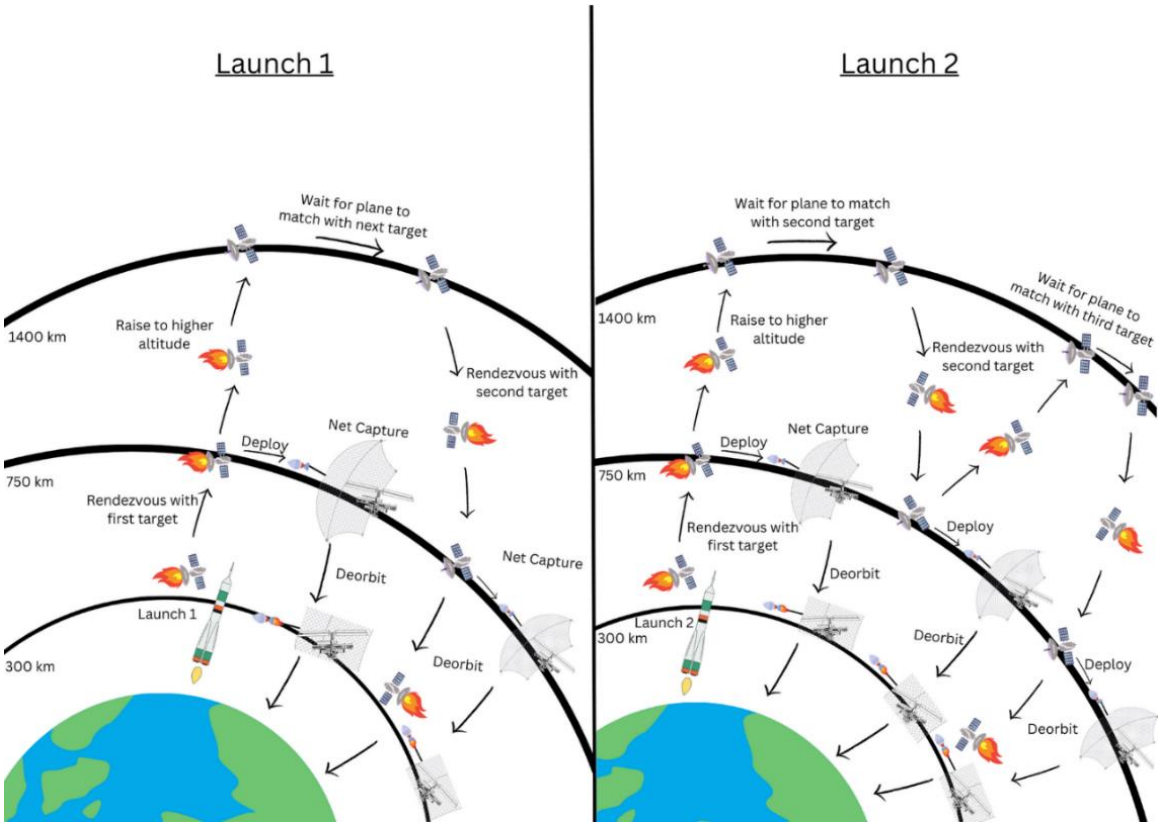

Figure 18: Mission Architecture 4. This mission architecture is composed of 2 separate launch vehicles each carrying a chaser. The first chaser is used to rendezvous with two target objects and the second chaser is used to rendezvous with the remaining three target objects, both chasers leveraging nodal precession.

Revisiting Table 15, target objects 1, 3, and 4 all seem to have relatively similar RAAN values with less than 30 deg. difference among all three target objects. These three targets can be grouped into the set of three, while the remaining two targets can be grouped into the set of two target objects. The set of two target objects have a difference of approximately 60 deg. in RAAN. Even though there is a large difference in RAAN between the set of two target objects, only a single RAAN plane match needs to be used that should keep the mission time under the one year rendezvous requirement (requirements can be reviewed in Fig. 3).

The order in which the chasers rendezvous with their target objects is important to ensure an optimal mission design. The ordering method will be identical to that discussed in mission architecture two. The first chaser will rendezvous with Target 2 and then with Target 5. The second chaser will rendezvous with Target 4, then Target 3, and finish with Target 1. The initial delta-v values were computed via the HPC script utilizing the Hohmann Transfer with plane change function (Table 18).

Table 18: Mission Architecture 4 Low Fidelity Analysis Results. Notice there are two launches. The first launch carries Chaser 1 that completes rendezvous with two target objects, and the second launch carries Chaser 2 that completes rendezvous with three target objects.

Launch	Target Number	ΔRAAN (deg.)	Approx. RAAN sync (days)	Raise Delta-v (m/s)	Rendezvous Delta-v (m/s)	Total Delta-v (m/s)
1	2	-	-	-	313.7	313.7
	5	59.6	238.4	296.4	312.1	608.5
Total	-	59.6	238.4	296.4	625.8	922.2
2	4	-	-	-	295.4	295.4
	3	25.2	101	293.3	310.7	604.0
	1	1.9	7.6	301.1	311.5	612.7
Total	-	27.1	108.6	594.4	917.6	1512.1
Mission Total						2434.3

The total delta-v of Chaser 1 and Chaser 2 were found to be 922.2 m/s and 1,512.1 m/s, respectively. A propellant mass check is essential to understand the feasibility of both chaser's total mass values. Using Eqn. 6, the propellant mass for Chaser 1 was estimated to be 5,373 kg which would result in a total mass of approximately 21,373 kg. This approximate total mass meets the launch vehicle's payload mass capability. The propellant

mass for Chaser 2 was estimated to be 9,722 kg resulting in a total mass of approximately 25,722 kg. This total mass approximation does not comply with the mass requirement. Additionally, the total RAAN sync time for both Chaser 1 and Chaser 2 were found to be 238.4 days and 108.6 days, respectively. The RAAN sync times for both chasers comply with the one year rendezvous requirement.

While Chaser 2 does not comply with the mass requirement, the total mass computation is an approximation based on different assumptions. The primary assumption that this approximation uses is a dry mass of 16,000 kg. Additionally, the dry mass is directly related to the propulsion mass of the chaser, so decreasing the dry mass would decrease the propellant mass which would significantly decrease the total mass of the chaser. Therefore, a study could be conducted to find a dry mass requirement given the relationship between the dry mass, propulsion mass, and the launch vehicle's payload mass requirement.

4.6 Mission Architecture Selection

The final mission architecture was selected to be mission architecture four. Mission architecture four was found to be the optimal design, among the four different architectures that were analyzed, based on the launch vehicle's payload mass capability, the ability to comply with the one year rendezvous requirement, and the single chaser design to decrease complexity. A higher fidelity analysis via STK was then used to gather more accurate timeline information and delta-v values using the low fidelity analysis values computed above as initial guesses.

The initialization for the two chasers followed the same process as in the STK implementation of mission architecture one. Chaser 1 was set to an altitude of 300 km, inclination of 98 deg., and a RAAN value of 113.796 deg. with an orbit epoch of January 27, 2028, 00:00:00.000 UTCG. Chaser 2 was set up identically, except for a RAAN value of 325.226 deg. with an orbit epoch of January 15, 2028, 00:00:00.000 UTCG. Both chasers were initially allocated a dry mass of 16,000 kg.

A mission control sequence was constructed for each of the chasers and their respective mission (Fig. 19). There are five primary segments in these mission control sequences apart from setting the initial state of each chaser. Additionally, each maneuver segment that will be discussed is assumed to be impulsive, which was selected within the maneuver segment settings, and the engine is set to the TR-312-100MN Dual Mode Liquid Apogee Engine.

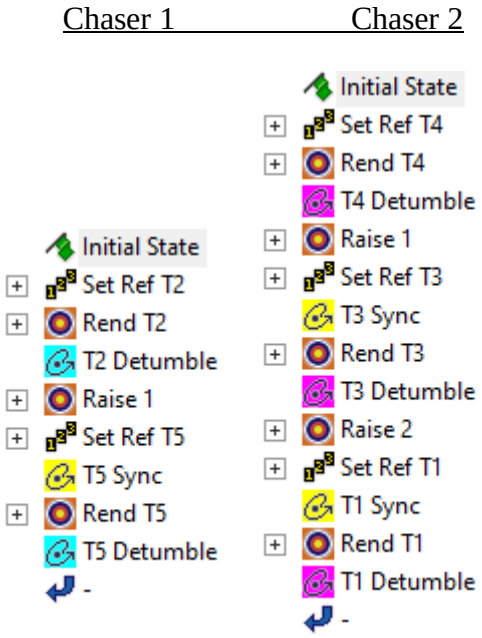

Figure 19: Selected Mission Architecture Mission Control Sequence.

"Set Ref T2" sets a particular target object, Target 2 in this instance, to be the chaser's reference vehicle. This is necessary to use the target's RIC frame to set the rendezvous relative position and velocities.

"Rend T2" is a target sequence that is used to perform the Lambert Search Profile to rendezvous with a particular targe object, in this case Target 2. This target sequence contains two propagate segments to find the wait time and time of flight, as well as two maneuver segments to find the thrust vectors for the rendezvous burns. The propagate segments use an Earth Point Mass propagator. The Lambert Search Profile utilizes a grid of search over one day with a five minute time step for rendezvous with Targets 2 and 4 with no phase match since the launch window would adjust for phase match. For Targets 5, 3, and 1, the Lambert Search Profile utilizes a grid search over three days with a five minute time step. Using a three day grid search helps to find the correct RAAN sync time while maintaining the same level of fidelity, a five minute time step. Additionally, the Lambert Search Profiles for rendezvous with Targets 5, 3, and 1 utilize a phase match since the chaser will be coming down from a raised orbit and need to account for additional delta-v that will be necessary for rendezvous with a target object.

"T2 Detumble" is a propagation segment that uses the user-defined propagator discussed previously to take into account orbital perturbations. The length of this propagation segment is set to 10 days to model an average time that it could take to detumble the target object, in this case Target 2, before the deorbit kit is deployed.

"Raise 1" is a differential corrector that raises the chaser's current orbit to the raised orbit. The differential corrector contains two maneuver segments that are applied along the velocity vector and one Earth Point Mass propagation segment for the time of flight. The

two maneuver segments and the time of flight are iterated until they converge on a solution to end in an orbit with an altitude of 1,400 km and eccentricity of zero.

"T5 Sync" is an additional propagation segment that utilizes the user-defined propagator to get the chaser and the next target object's orbital plane more aligned. This value was iterated using trial and error to find the best solution with the rendezvous segment that followed it. The iteration of the "Sync" duration stopping condition is necessary because this propagation segment considers more orbital perturbations than those used during the initial RAAN sync time calculation. The only orbital perturbation that was used for the initial RAAN sync time calculation was the Earth's oblateness effects.

The STK mission control sequences were executed, and values for RAAN sync time and delta-v were computed (Table 19). The total delta-v for Chaser 1 was found to be 1,106.11 m/s and that for Chaser 2 was found to be 2,065.38 m/s. These values are higher than the results previously discussed primarily due to the phase match that is needed in the noninitial rendezvous segments. Additionally, the total RAAN sync time was found to be approximately 229 days for Chaser 1 and 110 days for Chaser 2. Both total RAAN sync values are complying with the one year rendezvous mission requirement.

Table 19: Selected Mission Architecture STK Results. Notice an increase in the delta-v values for the STK results compared to the low fidelity analysis results since the rendezvous required a phase match for the non-initial rendezvous maneuvers.

Launch	Target Number	Rendezvous Day	Approx. RAAN sync (days)	Raise Delta-v (m/s)	Rendezvous Delta-v (m/s)	Total Delta-v (m/s)
1	2	January 27	-	-	302.62	302.62
	5	Sept. 22	229	308.65	494.84	803.49
Total	-		229	308.65	797.46	1106.11
2	4	January 15	-	-	275.76	275.76
	3	May 7	102.7	295.57	726.80	1022.37
	1	May 24	6.7	285.41	481.84	767.25
Total	-		109.4	580.98	1484.4	2065.38
Mission Total						3171.49

A plot of the altitude over time was generated for both chasers to illustrate the different maneuver and propagate segments and their corresponding timelines. Figure 20 shows the altitude changes over the mission timeline for Chaser 1, and Figure 21 shows the altitude changes over the mission timeline for Chaser 2. The increase from the initial orbit at 300 km to the rendezvous of the first target object and the rendezvous from the raised orbit to the next target object can be clearly visualized in both plots. Also, the detumbling propagations at the target object's altitudes and the RAAN sync time propagations at the raised orbit can be seen.

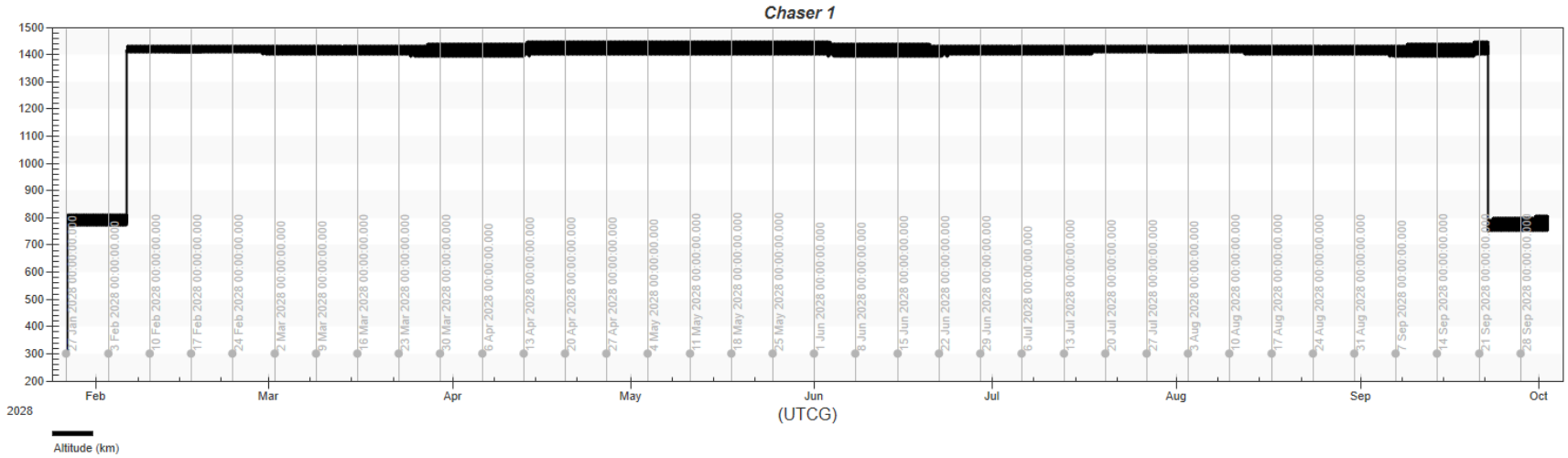

Figure 20: Chaser 1 Altitude Change Throughout Mission Timeline. Chaser 1 begins at the 300 km initial orbit, executes rendezvous maneuvers with the target objects around 800 km, and raises to the 1,400 km orbit to utilize the nodal precession.

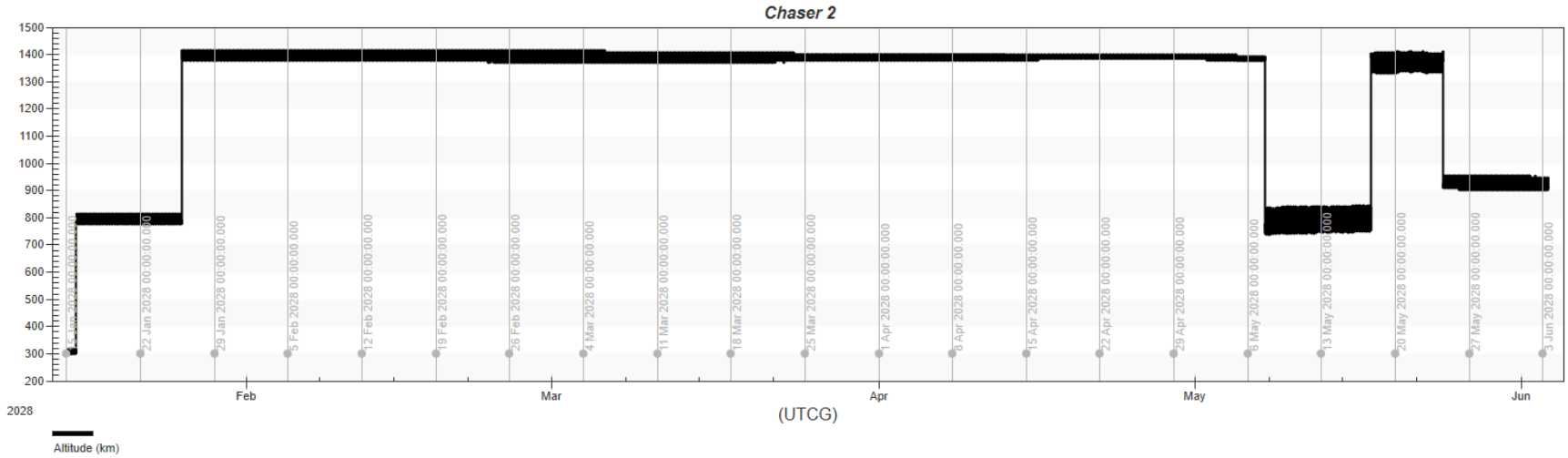

Figure 21: Chaser 2 Altitude Change Throughout Mission Timeline. Chaser 2 begins at the 300 km initial orbit, executes rendezvous maneuvers with the target objects around 800-900 km, and raises to the 1,400 km orbit to utilize the nodal precession.

A mass study is needed as previously discussed to find the maximum dry mass requirement for the chaser. Chaser 2 was investigated since it was evaluated to have the higher delta-v. The estimated fuel used for Chaser 2 in the analysis above was calculated to be 10,287.22 kg. This would amount to a total dry mass of over 26,000 kg thus surpassing the launch vehicle's payload mass capability. The same STK mission control sequences were re-run with different values of dry mass to find a relationship between the dry mass and the propellant mass. Eight different dry mass values were taken between 9,000 kg and 16,000 kg with a 1,000 kg increment. These dry mass values were set incrementally in Chaser 2's initial spacecraft parameters, and the corresponding estimated fuel mass values were computed (Table 20).

Table 20: Chaser 2 Fuel Mass Estimates for Given Dry Masses.

Dry Mass (kg)	16000	15000	14000	13000	12000	11000	10000	9000
Estimated Fuel Mass (kg)	10287	9663	9040	8416	7793	7169	6546	5922

The relationship between dry mass and the estimated fuel was found by plotting the data in Figure 22. The data was found to have an almost perfectly linear relationship, and a linear fit was applied. This linear relationship and the total mass requirement of 22,000 kg were used to create a system of equations in MATLAB. Solving this system of equations, a maximum dry mass was found to be 13,359 kg which corresponds with a propellant mass of 8,641 kg, hence totaling 22,000 kg. A 10% fuel reserve of 864 kg will be introduced which will also account for the end-of-life procedures for the chaser.

Adjusting the maximum dry mass and propellant mass results in 12,495 kg and 9,505 kg, respectively. This maximum dry mass value ensures that if a dry mass value is less than 12,495 kg, the propulsion that would be required to complete the mission would stay under the 22,000 kg requirement.

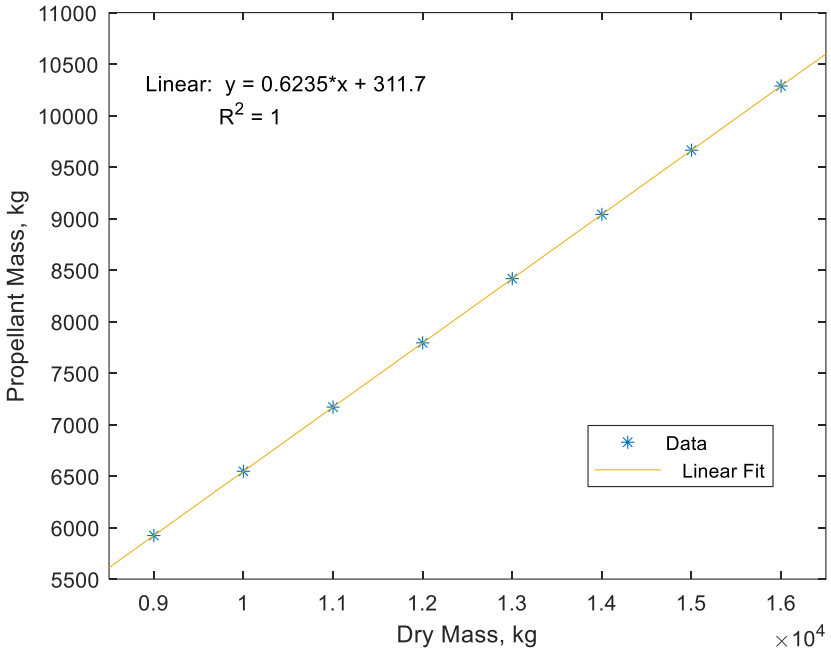

Figure 22: Relationship Between Propellant Mass and Dry Mass for Chaser 2.

The previous chapter analyzes different mission architectures using a low fidelity analysis. A final mission architecture is selected which is comprised of two launches containing two different chaser satellites. An approximate timeline, delta-v estimates, and a fuel requirement were developed for this given mission architecture. The next chapter will inspect the deorbit analysis which will be utilized after the deorbit kits have captured their designated target objects. This deorbit analysis is crucial in understanding the amount of delta-v and fuel that would be needed for the deorbit kits to deorbit all the target objects in a specified amount of time.

Chapter 5

Debris Deorbit Analysis

5.1 Deorbit Analysis Methodology

A deorbit analysis was conducted on the post-rendezvous portion of the mission to gain a more thorough understanding of the delta-v values that would be required from the deorbit kits. These deorbit kits, that will be deployed from the chaser, must contain enough fuel to perform a maneuver that will deorbit the target object in a specified amount of time. This analysis will assume that a single impulsive burn maneuver will be applied by the deorbit kit to find an approximate deorbit delt-v requirement. This will not consider a controlled reentry which would likely be needed in future works due to the high surface area and mass of the target objects. Even though a rendezvous architecture was selected in the previous section, this analysis starts at the net capture stage in the mission so the delta-v values can be true for any rendezvous architecture that would use a deorbit kit.

Identifying additional target object information was required to model the mission scenario more accurately. The maximum surface area and mass of each target object is very important since it is directly related to the amount of atmospheric drag that will be applied to the target object. These relationships can be seen mathematically by looking at the acceleration due to drag equation,

$$a_{\mathrm{d}} = \frac{1}{2}\frac{c_{\mathrm{d}}A}{m}\,\rho v^2 \tag{22}$$

where c_{d} is the coefficient of drag, A is surface area, m is mass, ρ is the atmospheric density, and v is the velocity of the object. This analysis assumes a spherical drag model with a coefficient of drag value of 2.2, which was proven to be a good approximation in the lower altitudes of LEO [43]. The atmospheric density is calculated using different atmospheric models, and the velocity of the object is dependent on the orbit that it is located in. Therefore, it was essential to define the surface area and mass of each target object (Table 21).

Table 21: Maximum Surface Area, Mass, and Area to Mass Ratio for Each Target [44][45][46][47][48].

Target	Mass (kg)	Maximum Surface Area (m^2)	Area to Mass Ratio (m^2/kg)
27386 ENVISAT	7800	260	0.03333
24277 ADEOS	3560	59	0.01657
27601 H-2A R/B	3000	36.8	0.01227
27597 ADEOS 2	3680	24	0.00652
27387 ARIANE 5 R/B	2575	18.36	0.00713

Furthermore, more information that was important for the deorbit analysis was the date that the deorbit kit would execute the deorbit maneuver and the target object's altitude at the start of the deorbit. The deorbit date was found in the rendezvous STK scenario timeline at the end of the detumbling propagation segment for each target object. This date corresponds to 10 days after the chaser rendezvous to give a window for detumbling and net capture. Knowledge of this date is important to establish the timeframes that each target

object must deorbit in. The starting altitude was initialized as the altitude of apoapsis on the specified deorbit date (Table 22).

Table 22: Target Object's Deorbit Dates and Starting Altitudes.

Target	Begin Deorbit Maneuver	Starting Altitude (km)
27386 ENVISAT	June 3	768.23
24277 ADEOS	February 6	802.72
27601 H-2A R/B	May 17	827.00
27597 ADEOS 2	January 25	808.47
27387 ARIANE 5 R/B	October 2	780.36

5.1.1 Low Fidelity Analysis

An initial deorbit analysis was conducted using the NASA Debris Assessment Software [35]. The goal of this initial analysis is to find the optimal decay lifetime of the target objects by investigating possible delta-v savings from extended decay lifetimes. A decay lifetime is the time that it takes for a specified object to decay through the atmosphere. Three different decay lifetimes were investigated: the first was to deorbit the target objects by the end of year (EOY), the second was one year, and the third was five years. The DAS software ingests the start year of the deorbit, the orbital lifetime, and the area to mass ratio of a target object. From these three parameters, the DAS software generates a plot of the delta-v required at different altitudes for the given input. An important note is that the software does not ingest an eccentricity of the target objects, so a circular orbit assumption is being used.

The EOY lifetime was found by finding the fraction of the year that remains after the deorbit maneuver is executed. The start year was set to 2028, the area to mass ratios were used from Table 21, and the plots were generated for all three decay lifetimes. The output from the one year orbital lifetime of Target 1, Envisat, can be seen in Figure 23. The line given in this output is the relationship between the starting altitude of the target object and the required delta-v that would be needed for deorbit.

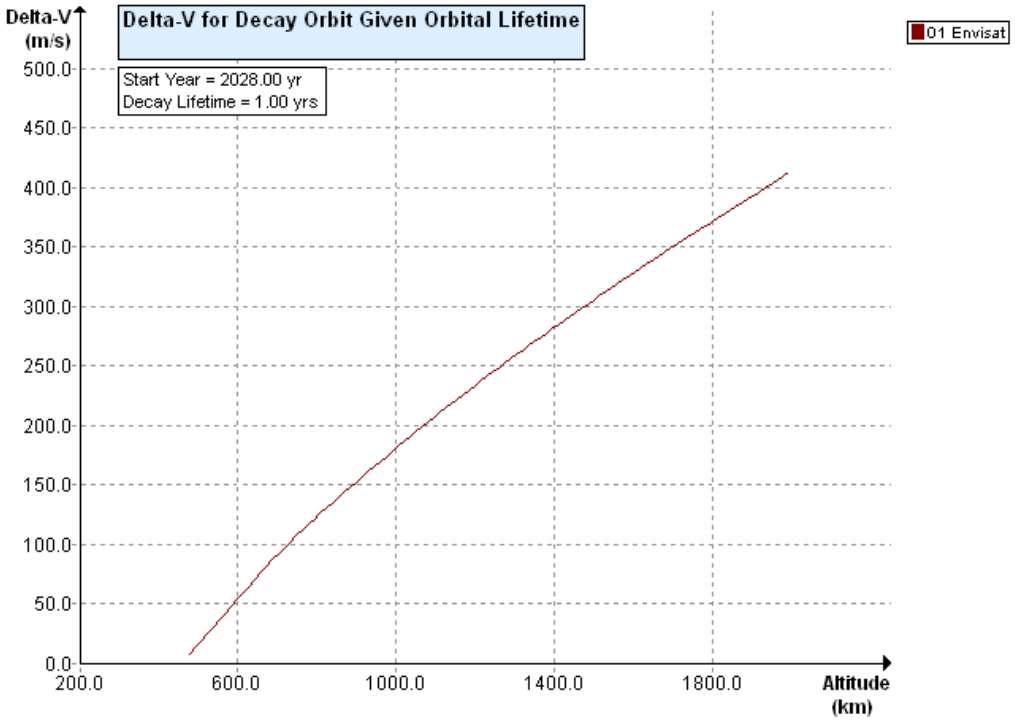

Figure 23: DAS Results for Envisat with a 1 Year Decay Lifetime.

The delta-v value at a specified altitude can be found using these plots. These delta-v values were recorded for each decay lifetime (Table 23). The highest delta-v requirement for deorbit was found to be 157 m/s which was associated with the EOY lifetime for Target 5. This is intuitive since it has the shortest amount of time to deorbit, which would generate a lower contribution from acceleration due to drag. Additionally, this target object had the

lowest mass and surface area compared to the other target objects. Target 4 had the lowest delta-v requirement in each decay lifetime due to its very large mass and surface area compared to the other target objects.

Table 23: Deorbit Results Using DAS. The delta-v requirements for each target object were computed for an EOY deorbit, a 1 year deorbit, and a 5 year deorbit.

Target	Starting Altitude (km)	Fraction of year until EOY	EOY Deorbit Delta-v (m/s)	1 year Deorbit Delta-v (m/s)	5 year Deorbit Delta-v (m/s)
1	768.23	0.5833	122	114	95
2	802.72	0.9167	137	136	117
3	827.00	0.6250	153	147	129
4	808.47	0.9167	151	150	133
5	780.36	0.2500	157	141	124

The EOY orbital lifetime was selected for further analysis. The largest delta-v savings between EOY orbital lifetime and the five year orbital lifetime was approximately 22%. This delta-v savings was not significant enough to extend the total mission duration four more years. The EOY orbital lifetime successfully maintains the shortest mission timeline while requiring reasonable delta-v values. Additionally, this orbital lifetime would conform to the recommendation set forth by Liou et al, which stated that five high priority orbital debris objects need to be deorbited per year to stabilize the LEO orbital debris population [10].

5.1.2 High Fidelity Analysis

A higher fidelity delta-v analysis was conducted using STK after the deorbit time was selected. An Astrogator mission control sequence was built to model this deorbit

segment (Fig. 24). The deorbit segment was modelled by creating a new satellite object, called a deorbit satellite, that was initialized at a slight offset, -5 meters in the in-track direction, from the desired target object's location with the target object's mass and surface area spacecraft parameters (Follow segment). Once the target object reached apogee on the maneuver date, a single impulsive burn was executed to reduce the deorbit satellite's perigee thus increasing the drag effects (Maneuver segment). These drag effects slowly circularize the orbit and continue to exponentially increase causing the satellite to deorbit (Propagate segment).

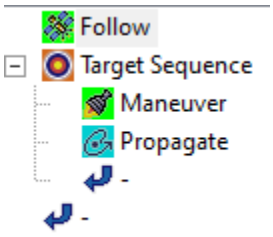

Figure 24: Deorbit Analysis Mission Control Sequence.

The propagation segment uses the same user-defined propagator that was developed in the rendezvous portion. This propagator uses an 18x18 gravitational force model while taking into account atmospheric drag, as well as third body effects from the Sun and Moon. The maneuver segment applies thrust in the anti-velocity direction using a set of four different attitude control thrusters. Different low thrust attitude control thrusters were compared, and the 10 N Bipropellant Thruster manufactured by EADS Astrium was selected to be used as the low thrust chemical engine model [35]. A set of four thrusters of this type would result in a 40 N thrust with an I_{sp} of 291 seconds using NTO and MMH as the propellant. Additionally, these thrusters are small with an engine mass and length of approximately 0.5 kg and 0.143 m, respectively.

The delta-v values in STK were found using a trial-and-error technique. The mission control sequence was executed for each target object with an initial guess for delta-v used from the results of the DAS analysis. An altitude report was generated, and the delta-v was either increased if no deorbit had occurred or the delta-v was decreased if the deorbit satellite had crashed into Earth. This process continued until a delta-v was found that would deorbit the satellite but not crash into the Earth as seen in Figure 25. It is assumed that the object could initiate a controlled re-entry at this point.

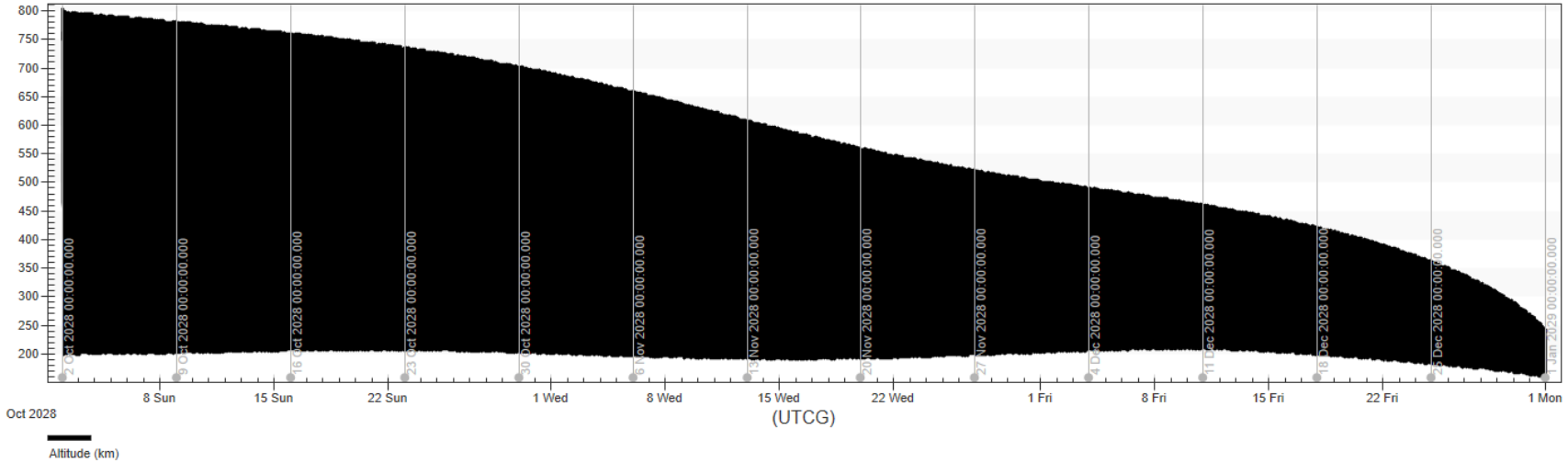

Figure 25: Altitude Plot of a Successfully Deorbited Target Object.

5.2 Deorbit Analysis Results

The delta-v values that were required to deorbit each target object are found in Table 24. The burn duration times, and estimated fuel usage were also recorded. The estimated burn durations provide an accuracy check of using an impulsive burn assumption since the thrusters can only provide 40 N of thrust. The largest estimated burn duration was found to be 6.88 hours which is low enough to verify the use of the impulsive burn assumption. The estimated fuel usage provides insight to the required sizing of the deorbit kits.

Table 24: Deorbit Results Using STK. These results display delta-v requirements for an EOY deorbit, the estimated fuel usage, and an estimated burn duration for each maneuver.

Target	EOY Deorbit Delta-v (m/s)	Approx. Fuel Used (kg)	Est. Burn Duration (hr.)
1	122	347.36	6.88
2	135	187.59	3.72
3	131	157.04	3.11
4	150	214.04	4.24
5	152	159.50	3.16

The delta-v values found in this analysis agree very closely with the delta-v values found using the Debris Assessment Software. The deorbit analysis for Target 3 disagrees the most from the DAS analysis. This inconsistency is possibly due to target objects higher starting altitude and eccentricity. The starting altitudes and eccentricities for each target object are recorded in Table 25 along with the difference between the DAS and STK delta-v values. Targets 3 and 5 have the two highest eccentricities which could be a primary

factor regarding the difference in the results because the DAS analysis assumes the target object is in a circular orbit.

Table 25: STK and DAS Results Comparison. A visualization of each target object's starting altitude and eccentricity is included to provide insight into the reasoning that some analyses display a larger difference in results.

Target	Starting Altitude (km)	Eccentricity	Diff w/ DAS (m/s)
1	768.23	0.001232	0
2	802.72	0.000880	2
3	827.00	0.007751	22
4	808.47	0.000920	1
5	780.36	0.002406	5

It is important to note that further research is required to identify the optimal placement of these four low thrust chemical engines on the deorbit kits. The exhaust plumes from these engines have the potential to burn through the space tether if positioned too closely. Also, these exhaust plumes could create a small force in the opposite direction of the motion on the targe object that is being removed. Angling these thrusters could alleviate these issues if they were found to be substantial.

5.3 End of Life

The end of life operations of each chaser object involve a slow deorbit into the atmosphere themselves. The DAS software was used to find approximate delta-v reserves that are needed for the chaser satellites to ensure that they can perform a final maneuver after all the desired targets have been captured. These procedures are in compliance with the five year post-mission disposal timeline that is now a requirement for LEO satellites

[49]. The chaser satellites were assumed to have an area of 20 m^2 and a final mass was used from the maximum dry mass requirement found above of 12,495 kg. The area to mass ratio was found to be 0.0016 m^2/kg for the chaser satellites.

Using these area to mass ratios, a start year of 2028, and a decay lifetime of five years, the required delta-v was computed for each chaser. Chaser 1's last target object is Target 5 which is located to be at an altitude of approximately 780.36 km, and Chaser 2's last target object is Target 1 at an altitude of approximately 768.23 km. Using these starting altitudes, Chaser 1 and Chaser 2 were estimated to need 143 m/s and 140 m/s of delta-v, respectively. The propellant mass can be found from these dela-v values. The rocket equation that was rearranged to solve for the propellant mass is revisited,

$$m_{\text{prop}} = m_{\text{f}} \exp\left(\left(\frac{\Delta v_{\text{tot}}}{I_{\text{sp}} * g_{\text{o}}}\right) - 1\right) \tag{23}$$

The I_{sp} of the chaser's primary engine, which will be used for the end of life maneuver, is 325 seconds. This maneuver will act in the anti-velocity direction similarly to the deorbit kits. Solving the propellant mass equation above finds the required propellant mass to execute Chaser 1's end of life maneuver to be 574 kg and Chaser 2's end of life maneuver to be 561 kg. These maneuvers are within the given propellant mass allotment of 864 kg, which was given above.

Chapter 6

Discussion

6.1 Delta-v Budget

The delta-v required for a mission is critical to understand. The delta-v can be broken up into its different maneuvers for easier visualization using a delta-v budget. A delta-v budget for each of the chaser objects is shown in Table 26. The delta-v maneuvers that are listed in this table relate to the rendezvous and raise segments that are used to sequentially rendezvous with the different target objects. Chaser 1 only displays two rendezvous segments with one raise segment in between since it is only required to rendezvous with Targets 2 and 5. Chaser 2 displays three different rendezvous segments with two raise segments in between since it is targeting objects 4, 3, and 1. Additionally, the end of life maneuver is included which is used to deorbit the two chasers after their mission is complete to comply with current disposal guidelines. The total delta-v that is required from Chaser 1 was found to be 1,249.11 m/s, and the required delta-v for Chaser 2 was found to be 2,205.38 m/s. Note that additional delta-v could be necessary for station keeping which are small corrective maneuvers that are used to correct deviations that could develop in the chaser's orbit. The delta-v that would be required for these maneuvers is estimated to be

very small with respect to that required for the other maneuvers and is thus excluded from this delta-v budget.

Table 26: Delta-V Budget of Chasers 1 and 2. This delta-v budget takes into account all of the rendezvous, raise, and disposal maneuvers required for each chaser.

Maneuver	Chaser 1	Chaser 2
Rendezvous 1	302.62 m/s	275.76 m/s
Raise 1	308.65 m/s	295.57 m/s
Rendezvous 2	494.84 m/s	726.80 m/s
Raise 2	-	285.41 m/s
Rendezvous 3	-	481.84 m/s
Disposal (EOL)	~143 m/s	~140 m/s
Total	1249.11 m/s	2205.38

6.2 Mass Budget

The estimated mass distribution of the two chaser satellites is shown in a mass budget (Table 27). These masses and their percentages can prove to be very useful when moving to the spacecraft design phase. The relationship between the dry mass and the propellant mass has already been investigated. For this mission, the maximum dry mass was found to be 12,495 kg. The propellant mass that would be required to maneuver a chaser at this maximum dry mass, while not exceeding the launch vehicle's payload mass limit, would be 9,505 kg. Subsystem average masses for a LEO mission were found as a function of dry mass [35]. Using these percentages with the maximum dry mass found for this mission can generate an estimated value for the maximum allowable mass for each subsystem.

Table 27: Mass Budget with Total Mass Percentages.

Subsystem	Percentage	Mass (kg)
Payload	18%	3872
Structure and Mechanisms	15%	3374
Thermal Control	1%	250
Power	12%	2624
TT&C	1%	250
On-Board Processing	3%	625
Attitude Determination and Control	3%	750
Propulsion	2%	375
Reserves	2%	375
Propellant	43%	9505
Total	100.00%	22000

Using the mass budget, the estimated maximum mass for the payload is found to be 3,872 kg. The payload for this mission includes a laser system to be used for detumbling of the object, the net capture system, and up to three deorbit kits for the target object removal. The maximum payload mass gives a baseline as to the mass requirements that these different systems would need to meet. Additionally, the different subsystems can be investigated with an estimation for each subsystem's maximum allowable mass.

6.3 Conclusions

The three primary trade studies sought to identify a set of target objects, an ADR method, and a mission architecture. The purpose of this mission preliminary mission design is to combine current ADR technologies and research to begin to generate a feasible ADR mission. The growing orbital debris population found in LEO continues to illustrate the

call for immediate action. Many researchers are completing extensive work regarding the classification of target object, different ADR capture and removal methods, and detumbling techniques. It is necessary to begin to combine the knowledge that is currently available and begin to form ADR missions that could be implemented in the near future.

This analysis is an attempt to combine many different aspects of an ADR mission to provide initial results and approximate calculations that could be required for the execution of a useful ADR mission. The requirements that were used throughout each trade study emphasize the need for a low-cost mission with a short mission timeline that can be executed with minimal legal barriers. Therefore, the results of these trade studies can be further developed in the future so that an effective ADR mission can be implemented to stabilize the growth of the LEO debris object population.

The set of target objects that was selected were five debris objects found to be in the significantly most concerning LEO debris object list. All five of these selected target objects originated from a state that have current space partnerships so that there would be minimal legal issues with their removal. The ADR capture, removal, and detumbling methods were analyzed by comparing them against one another to find a method that has been extensively developed, minimizes the risk of the creation of additional debris objects, and can be executed on a wide variety of target objects. The selection of a net capture method was found to be the best capture method since it can target large, tumbling objects as well as it can be used at distance from the target object to reduce the risk of collision. Low thrust chemical engines were selected to be used for the removal method. This removal method is a low-risk option that creates a smaller force on the space tether, which is attached to the target object using the net capture system, and solar panels that may be

present on the chaser compared to a higher thrust chemical system. Additionally, the use of a detumbling method is critical due to the low accuracy that current methods have on measuring space debris' tumbling rates. Detumbling the target objects via laser ablation was selected since it has been extensively researched and has shown successful results via numerical simulations [29].

The orbital analysis was used to analyze different mission architectures and give approximate calculations for timelines, orbital maneuvers, and mass estimates. A final mission architecture was chosen that satisfies a low number of chasers to minimize the launch cost, and to utilize the nodal precession for plane changes. There is a very large fraction of a mission's costs that are historically used for launch costs. By choosing a low-cost launch vehicle, the Falcon 9, and by minimizing the number of required launches, the total launch costs that would be required for this mission were significantly reduced.

The delta-v, mission timeline, and mass distributions that were calculated for the selected mission architecture provide initial approximations for the requirements of an ADR mission of this type. The results found in the trade studies used above develop a mission architecture that combines decades of research in the orbital debris mitigation field and is focused on a mission that could be implemented in the near future. Development of these architecture, and other research that looks to combine current ADR techniques, are essential to begin to stabilize the LEO space debris environment.

6.4 Future Work

Many different areas of future work are necessary to continue to develop a highly effective ADR mitigation mission that can be implemented in the near future. Investigating

a new set of target objects that can further take advantage of nodal precession could potentially reduce the required number of launches down to one. This set of target objects should continue to investigate high priority objects, but it should also investigate targets that are similar in RAAN to use the natural RAAN drift. Additionally, it would be advantageous to investigate the legal concerns if a target object that originated from the CIS was chosen since these objects were found to be among the primary group in the statistically most concerning (SMC) object list.

The advancement in current ADR technologies as well as the investigation into new ADR technologies are important. The current ADR technology research can continue to increase their respective TRL, so that this technology can be used with minimal research and development cost if chosen for an ADR mission. Further investigations in the measurements of space debris tumbling rates will be a key component to future ADR missions. The required detumbling technology and timeline with respective to a given set of target objects could be more detailed, if an accurate measurement of space target tumbling rates could be measured. The selected set of target objects could additionally not require detumbling technology if these values were accurate and in-situ measurements were not needed.

The extension of this mission architecture such as mission design, chaser design, and deorbit kit design is essential to allow for near future implementation. The exact design of the chasers and deorbit kits can begin to be developed from initial mass requirements that were developed in the analyses presented here. The delta-v calculations will need to be re-investigated using higher fidelity propagators and trajectory optimizers due to the simplifying assumptions made here. The presented mission design provides useful

information regarding different mission design phases which motivates the continuation of work to further develop the requirements and mission architecture to implement an ADR mitigation mission.

Bibliography

[1] Garcia, M., “Space debris and human spacecraft,” *NASA* Available: https://www.nasa.gov/mission_pages/station/news/orbital_debris.html.

[2] Kessler, D. J., and Cour-Palais, B. G., “Collision Frequency of Artificial Satellites: The Creation of a Debris Belt,” *Journal of Geophysical Research*, vol. 83, 1978, pp. 2637–2646.

[3] United Nations, "Space Debris Mitigation Guidelines of the Committee on the Peaceful Uses of Outer Space," 2010

[4] U.S. Government, "Orbital Debris Mitigation Standard Practices," November 2019 Update

[5] Inter-Agency Space Debris Coordination Committee, “IADC Space Debris Mitigation Guidelines,” Mar. 2020.

[6] Iridium, SPACEX, and OneWeb, “Satellite Orbital Safety Best Practices,” Sep. 2022.

[7] Sánchez-Arriaga, G., Sanmartín, J. R., and Lorenzini, E. C., “Comparison of technologies for deorbiting spacecraft from low-earth-orbit at end of mission,” *Acta Astronautica*, vol. 138, 2017, pp. 536–542.

[8] Mason, J., Stupl, J., Marshall, W., and Levit, C., “Orbital debris–debris collision avoidance,” *Advances in Space Research*, vol. 48, 2011, pp. 1643–1655.

[9] Liou, J.-C., Johnson, N. L., and Hill, N. M., “Controlling the growth of future LEO debris populations with active debris removal,” *Acta Astronautica*, vol. 66, 2010, pp. 648–653.

[10] Liou, J.-C., “An active debris removal parametric study for LEO environment remediation,” *Advances in Space Research*, vol. 47, 2011, pp. 1865–1876.

[11] Covello, F., “Application of electrical propulsion for an active debris removal system: a system engineering approach,” *Advances in Space Research*, vol. 50, 2012, pp. 918–931.

[12] Tadini, P., Tancredi, U., Grassi, M., Anselmo, L., Pardini, C., Francesconi, A., Branz, F., Maggi, F., Lavagna, M., DeLuca, L. T., Viola, N., Chiesa, S., Trushlyakov, V., and Shimada, T., “Active debris multi-removal mission concept based on hybrid propulsion,” *Acta Astronautica*, vol. 103, 2014, pp. 26–35.

[13] Olympio, J. T., and Frouvelle, N., “Space debris selection and optimal guidance for removal in the SSO with low-thrust propulsion,” *Acta Astronautica*, vol. 99, 2014, pp. 263–275.

[14] Visagie, L., Lappas, V., and Erb, S., “Drag sails for space debris mitigation,” *Acta Astronautica*, vol. 109, 2015, pp. 65–75.

[15] Baranov, A. A., Grishko, D. A., Razoumny, Y. N., and Jun, L., “Flyby of large-size space debris objects and their transition to the disposal orbits in LEO,” *Advances in Space Research*, vol. 59, 2017, pp. 3011–3022.

[16] Yang, J., Hu, Y. H., Liu, Y., and Pan, Q., “A maximal-reward preliminary planning for multi-debris active removal mission in LEO with a greedy heuristic method,” *Acta Astronautica*, vol. 149, 2018, pp. 123–142.

[17] Anselmo, L., and Pardini, C., “Ranking upper stages in low Earth orbit for active removal,” *Acta Astronautica*, vol. 122, 2016, pp. 19–27.

[18] Borelli, G., Trisolini, M., Massari, M., and Colombo, C., “A Comprehensive Ranking Framework for Active Debris Removal Missions Candidates,” *8th European Conference on Space Debris*, 2021.

[19] McKnight, D., Witner, R., Letizia, F., Lemmens, S., Anselmo, L., Pardini, C., Rossi, A., Kunstadter, C., Kawamoto, S., Aslanov, V., Dolado Perez, J.-C., Ruch, V., Lewis, H., Nicolls, M., Jing, L., Dan, S., Dongfang, W., Baranov, A., and Grishko, D., “Identifying the 50 statistically-most-concerning derelict objects in LEO,” *Acta Astronautica*, vol. 181, 2021, pp. 282–291.

[20] Biesbroek, R., Soares, T., Husing, J., and Innocenti, L., “The E.DEORBIT CFD Study: A Design Study for the Safe Removal of a Large Space Debris,” *6th European Conference on Space Debris*, 2013, pp. 1–8.

[21] Kawamoto, S., Nagaoka, N., Kitagawa, Y., Harada, R., and Hanada, T., “Considerations on the lists of the top 50 debris removal targets,” *Journal of Space Safety Engineering*, vol. 9, 2022, pp. 455–463.

[22] White, A. E., and Lewis, H. G., “The many futures of active debris removal,” *Acta Astronautica*, vol. 95, 2014, pp. 189–197.

[23] Shan, M., Guo, J., and Gill, E., “Review and comparison of active space debris capturing and removal methods,” *Progress in Aerospace Sciences*, vol. 80, 2016, pp. 18–32.

[24] Forshaw, J. L., Aglietti, G. S., Navarathinam, N., Kadhem, H., Salmon, T., Pisseloup, A., Joffre, E., Chabot, T., Retat, I., Axthelm, R., Barraclough, S., Ratcliffe, A., Bernal, C., Chaumette, F., Pollini, A., and Steyn, W. H., "RemoveDEBRIS: An in-orbit active debris removal demonstration mission," *Acta Astronautica*, vol. 127, 2016, pp. 448–463.

[25] Benvenuto, R., Salvi, S., and Lavagna, M., "Dynamics analysis and GNC design of flexible systems for space debris active removal," *Acta Astronautica*, vol. 110, 2015, pp. 247–265.

[26] Hakima, H., and Emami, M. R., "Assessment of active methods for removal of LEO debris," *Acta Astronautica*, vol. 144, 2018, pp. 225–243.

[27] Ledkov, A., and Aslanov, V., "Review of contact and contactless active space debris removal approaches," *Progress in Aerospace Sciences*, vol. 134, 2022, pp. 1–19.

[28] Lampariello, R., "On Grasping a Tumbling Debris Object with a Free-Flying Robot," *IFAC Proceedings*, vol. 46, 2013, pp. 161–166.

[29] Vetrisano, M., Thiry, N., and Vasile, M., "Detumbling Large Space Debris via Laser Ablation," *2015 IEEE Aerospace Conference*, 2015.

[30] Sagnières, L. B., and Sharf, I., "Long-Term Rotational Motion Analysis and Comparison to Observations of the Inoperative Envisat," *Journal of Guidance, Control, and Dynamics*, vol. 42, 2019, pp. 364–376.

[31] Schildknecht, T., Krag, H., and Flohrer, T., "Determining, Monitoring and Modelling the Attitude Motion of Potential ADR Targets," *Clean Space Industrial Days*, May 2016.

[32] Mehrholz, D., Leushacke, L., Flury, W., Jehn, R., Klinkrad, H., and Landgraf, M., "Detecting, Tracking and Imaging Space Debris," *esa* Available: https://www.esa.int/esapub/bulletin/bullet109/chapter16_bul109.pdf.

[33] "RObotic GEostationary orbit Restorer (Roger)," *ESA* Available: https://www.esa.int/Enabling_Support/Space_Engineering_Technology/Automation_and_Robotics/RObotic_GEostationary_orbit_Restorer_ROGER.

[34] Chu, Z., Di, J., and Cui, J., "Hybrid tension control method for tethered satellite systems during large tumbling space debris removal," *Acta Astronautica*, vol. 152, 2018, pp. 611–623.

[35] Everett, D. F., Wertz, J. R., and Puschell, J. J., *Space Mission Engineering: The New SMAD*, Torrance, CA: Microcosm Press, 2018.

[36] "Falcon 9," *Wikipedia* Available: https://en.wikipedia.org/wiki/Falcon_9.

[37] "Propagators," *STK Help* Available: https://help.agi.com/stk/11.0.1/Content/gator/ab-prop.htm.

[38] Bate, R. R., Mueller, D. D., and White, J. E., *Fundamentals of Astrodynamics*, Dover Publications, Inc., 1971.

[39] Arora, N., and Russell, R. P., "A Fast And Robust Multiple Revolution Lambert Algorithm Using A Cosine Transformation," *Advances in the Astronautical Sciences*, vol. 150, 2014, pp. 411–430.

[40] Montenbruck, O., and Gill, E., *Satellite Orbits Models, Methods and Applications*, Springer, New York, 2012.

[41] Smeltzer, S., and Wagner, N., "De-Orbit Analysis using Active Debris Removal for High Priority Objects," *AIAA ASCEND 2022*, 2022. https://doi.org/10.2514/6.2022-4275.

[42] Baranov, A. A., Grishko, D. A., and Razoumny, Y. N., "Large-Size Space Debris Flyby in Low Earth Orbits," *Cosmic Research*, vol. 55, 2017, pp. 361–370.

[43] Cook, G. E., "Satellite Drag Coefficients," *Planetary and Space Science*, vol. 13, 1965, pp. 929–946.

[44] "Envisat," *Wikipedia* Available: https://en.wikipedia.org/wiki/Envisat.

[45] "ADEOS I," *Wikipedia* Available: https://en.wikipedia.org/wiki/ADEOS_I.

[46] "H-IIA," *Wikipedia* Available: https://en.wikipedia.org/wiki/H-IIA.

[47] "ADEOS II," *Wikipedia* Available: https://en.wikipedia.org/wiki/ADEOS_II.

[48] "Ariane 5," *Wikipedia* Available: https://en.wikipedia.org/wiki/Ariane_5.

[49] Foust, J., "FCC approves new orbital debris rule," *SpaceNews* Available: https://spacenews.com/fcc-approves-new-orbital-debris-rule/#:~:text=Under%20the%20new%20rule%2C%20spacecraft,the%20end%20of%20their%20mission.